**FABRICATION AND COLD-FLOW TESTING
OF SUBSCALE SPACE-BASED LASER
GEOMETRY**

THESIS

Scott E. Bergren, Captain, USAF

AFIT/GAE/ENY/02-3

**DEPARTMENT OF THE AIR FORCE
AIR UNIVERSITY**

AIR FORCE INSTITUTE OF TECHNOLOGY

Wright-Patterson Air Force Base, Ohio

Report Documentation Page

Report Date	Report Type	Dates Covered (from... to)
26 Mar 2002	Final	Aug 2000 - Mar 2002

Title and Subtitle Fabrication and Cold-Flow Testing of Subscale Space-Based Laser Geometry	**Contract Number**
	Grant Number
	Program Element Number
Author(s) Capt Scott E. Bergren	**Project Number**
	Task Number
	Work Unit Number
Performing Organization Name(s) and Address(es) Air Force Institute of Technology Graduate School of Engineering and Management (AFIT/EN) 2950 P Street WPAFB OH 45433-7765	**Performing Organization Report Number** AFIT/GAE/ENY/02-3
Sponsoring/Monitoring Agency Name(s) and Address(es) Capt Matthew Zuber SMC/TL 2420 Vela Way, Suite 1467-80 Los Angeles, CA 90245-4659	**Sponsor/Monitor's Acronym(s)**
	Sponsor/Monitor's Report Number(s)

Distribution/Availability Statement
Approved for public release, distribution unlimited

Supplementary Notes

Abstract
The objectives of this research were to build a facility that could simulate the expected fluid flow properties in the conceptual Space Based Laser Integrated Flight Experiment (SBL IFX) gas dynamic laser using cold-flow, and to investigate the performance of the model. A 1/5-scale model of one quadrant of the SBL IFX cylindrical, gas dynamic laser was fabricated and mated to a blow-down/vacuum combination wind tunnel. The primary components of the test apparatus consisted of a nozzle array, optical cavity, supersonic diffuser, centerbody, and transition. The throat height of a single nozzle was 1 mm and the expansion ratio was two. The transition structure was designed to attach the subscale model to the wind tunnel facility vacuum line and was not part of the SBL IFX design.

Subject Terms
Space Based Laser, Supersonic Diffuser, Fluid Dynamics, Compressible Flow, Schlieren Photography, Blow-Down Wind Tunnel, Transient Behavior

Report Classification unclassified	**Classification of this page** unclassified

Classification of Abstract unclassified	**Limitation of Abstract** UU
Number of Pages 106	

AFIT/GAE/ENY/02-3

FABRICATION AND COLD-FLOW TESTING OF SUBSCALE SPACE-BASED
LASER GEOMETRY

THESIS

Presented to the Faculty

Department of Aeronautical and Astronautical Engineering

Graduate School of Engineering and Management

Air Force Institute of Technology

Air University

Air Education and Training Command

In Partial Fulfillment of the Requirements for the

Degree of Master of Science in Aeronautical Engineering

Scott E. Bergren, B.S.

Captain, USAF

March 2002

FABRICATION AND COLD-FLOW TESTING OF SUBSCALE SPACE-BASED
LASER GEOMETRY

Scott E. Bergren, BS
Captain, USAF

Approved:

_____
Milton E. Franke (Chairman)

12 Mar 2002
date

_____
Lt Col Montgomery C. Hughson (Member)

12 MAR '02
date

_____
Major Jeffery P. Bons (Member)

12 Mar 2002
date

Acknowledgments

Table of Contents

List of Figures

List of Tables

List of Symbols

Symbol	Definition	Units

English Notation

Symbol	Definition	Units
A	cross-sectional area, perpendicular to flow	m
a	speed of sound	m/s
B	bias error	
D	diameter	m
f	Darcy friction factor	
h	head loss	m^2/s^2
K	loss coefficient	
L	length	m
M	Mach number	
$\dot{m}$	mass flow	kg/s
p	pressure	Pa
R	universal gas constant	kJ/kgK
S	precision index, reference temperature	K
T	temperature	K
t	Student's t-distribution function	
u	x-direction component of velocity	m/s
v	y-direction component of velocity	m/s
V	velocity	m/s
w	uncertainty	

Greek Notation

Symbol	Definition	Units
γ	ratio of specific heats	
ρ	density	kg/m^3
ν	kinematic viscosity	m^2/s
μ	absolute viscosity	Ns/m^2
Λ	volume	m^3

Subscripts/Superscripts

Symbol	Definition
*	critical dimension
t	stagnation
T	combined (total)
1	upstream location

2	downstream location
e	equivalent, expansion
c	contraction
l	loss
$throat1$	nozzle throat
$throat2$	diffuser throat
$-$	average
h	wetted

AFIT/GAE/ENY/02-3

Abstract

The objectives of this research were to build a facility that could simulate the expected fluid flow properties in the conceptual Space Based Laser Integrated Flight Experiment (SBL IFX) gas dynamic laser using cold-flow, and to investigate the performance of the model. A 1/5-scale model of one quadrant of the SBL IFX cylindrical, gas dynamic laser was fabricated and mated to a blow-down/vacuum combination wind tunnel. The primary components of the test apparatus consisted of a nozzle array, optical cavity, supersonic diffuser, centerbody, and transition. The throat height of a single nozzle was 1 mm and the expansion ratio was two. The transition structure was designed to attach the subscale model to the wind tunnel facility vacuum line and was not part of the SBL IFX design.

Using rapid data acquisition and schlieren photography, the fluid velocities in the diffuser where determined to became subsonic after a transient time interval of 0.2 seconds from wind tunnel startup for a 30 second long test. During this transient time interval, a well-defined, attached oblique shock wave was observed off the leading edge of the centerbody within the optical cavity of the diffuser, and the fluid in the optical cavity reached an observed maximum Mach number of 2.7. The brevity of the supersonic flow within the optical cavity was due to the minimum area of the transition structure being too small to "swallow" a normal shock that propagates down the length of the test section during a transient time period at wind tunnel startup.

FABRICATION AND COLD-FLOW TESTING OF SUBSCALE SPACE-BASED LASER GEOMETRY

1. Introduction

1.1 Background

Research into gas dynamic lasers (GDL) has slowed since the end of the Star Wars program in the late 1980's for the purposes of developing a space-based defense network. However, new life has been breathed into such research as a result of a U.S. Air Force and Ballistic Missile Defense Organization contract with an industry joint venture for the Space Based Laser Integrated Flight Experiment (SBL IFX) in 1999. Lockheed Martin Corporation, The Boeing Company, and TRW, Inc form the joint venture. The SBL IFX will prove the technology necessary for a network of satellites to utilize multi-megawatt power, cylindrical, GDLs to destroy ballistic missiles in their boost phase of flight, once in the upper atmosphere. The fluid dynamics internal to this high power GDL is the focus of this study.

The power generated in the SBL IFX is a result of an exothermic reaction of hydrogen and dissociated fluorine. This reaction creates vibrationally excited hydrogen-fluoride (HF) gas that generates the needed population inversion necessary for lasing (11). A cylindrical array of nozzles accelerates the dissociated fluorine supersonically. In the diverging portion of the nozzles, hydrogen is injected into the fluorine flow and the chemical reaction begins just after the nozzle exit plane.

The need for supersonic flow is three fold (11):

1) The chemical reaction needs to occur quickly for lasing to occur. The faster the mixing times the quicker the chemical reaction.

2) High temperatures destroy the lasing process. Isentropic, supersonic expansion is a way to cool a fluid and produce the temperatures conducive for lasing.

3) The faster the fluid is moving, the more power ultimately that can be extracted from the fluid flow.

The flow structure in the nozzles, lasing cavity, and the diffuser are critical to the laser performance. The beam quality is strongly dependent on the homogeneity of the lasing medium. Shock waves and boundary layer separation in the lasing cavity are sources of beam distortion and result in less power that can be extracted from the laser (3:12).

Cylindrical laser designs evolved to achieve compactness and to replace the extremely long and heavy linear diffusers required to overcome the complexities of mixing jets from nozzle clusters, wall boundary effects, and shock interaction effects (7:1). As a result, the size of a cylindrical laser makes it ideally suited for payload packaging for airlift and space applications.

1.2 Problem Statement

TRW is responsible for the power generation portion of the SBL IFX. This segment of the SBL IFX is where the population inversion occurs causing the initial lasing. Currently, TRW has designed a nozzle array and diffuser that will theoretically create a laser in the megawatt class. Two-dimensional, computational fluid dynamics by TRW has yielded preliminary results for the performance of the purposed design.

Experimental data are desired to verify the current computational results. A model of the proposed design can be created to examine the flow characteristics, which can determine the effectiveness of the laser.

1.3 Objective

This research effort has two major objectives:

1. To design and build a facility capable of investigating flow conditions in a simulated laser nozzle assembly and lasing cavity using cold-flow. This facility was designed to be modular for the purposes of testing various geometries.

2. Based on the time history of pressures in the diffuser and schlieren photography of the flowfield, determine the operating characteristics of the nozzle/diffuser system.

The first objective was accomplished by building a one-fifth scale, 90 deg segment of the proposed TRW laser generator and adapting the model to an existing blow-down wind tunnel. A considerable amount of design work was undertaken to scale and incorporate the model into the existing facility.

The second objective was satisfied by an analysis of static pressure data and schlieren photography. When analyzing the results, shock wave patterns and regions of separation were of key interest.

1.4 Summary of Current Knowledge

Current knowledge of GDLs has matured through the development of the Airborne Laser (ABL) by the Air Force. The ABL is a theater defense system designed to kill tactical ballistic missiles, which could possibly be carrying chemical and biological weapons. It is expected to be operational in the year 2008 (11). In earlier work in the late 1970s and early 1980s, the United States Air Force Weapons Laboratory (AFWL)

performed research on an experimental chemical GDL that had a cylindrical geometry for the purpose of ultimately using it in an airborne application. United Technologies Research Corporation (UTRC) was contracted to investigate large losses in total pressure associated with an unstarting phenomenon with the radial diffuser (18:2-3). From 1979 to 1984, Zumpano and Guile of UTRC experimentally investigated radial diffuser configurations relevant to the Air Force's research at the time. In the final UTRC technical report, the purpose of the radial diffuser research was encapsulated:

> The objective of this program was to develop the pressure-recovery technology necessary for stable operation of a compact radial-flow diffuser for airborne applications of high power chemical laser systems. (18:1)

By performing cold-flow tests on a 1/5-scale model of the full size radial diffuser, UTRC used various configurations and flow control techniques to optimize the flow. Good similarity of the subscale model to the actual device was accomplished by scaling the flow rate on a mass flux basis. Both Reynolds number and Mach number matched the estimated full-scale values (18:299).

In 1990, a numerical solution of the supersonic flow through a radial diffuser was successfully accomplished for the first time. This was accomplished by incorporating a modified two-layer Cebeci-Smith algebraic eddy viscosity turbulence model into the compressible Navier-Stokes equations (7).

Since the SBL IFX contract with industry was formed in 1999, no additional experimental testing has been performed on cylindrical diffusers for the purpose of a space application. Computer modeling has been performed by TRW for two-dimensional flow and the results indicated sensitivity to boundary layer separation with small changes in back pressure in the lasing cavity, between the nozzles and the diffuser. Furthermore,

the computer generated results determined the lasing cavity was absent of shock structures that may degrade laser power performance (14).

1.5 Method

In order to accomplish the first objective, a scaled design of the proposed model was required. The following questions were asked:

1) What scale model should be created?

2) What design/shape should nozzles be to meet the desired exit Mach number into the lasing cavity and reduce the manufacturing time?

3) To achieve modularity, how will the nozzle assembly mate to the diffuser?

4) How will the entire test section be connected to the existing plumbing of the current wind tunnel?

Once the model was built, the following general method was used to ultimately collect the necessary information to make conclusions about the model's performance. The following steps were used:

1) Run the wind tunnel at combinations of reservoir pressure, to alter the mass flow and possible regions of separation

2) Record wall static pressure along the length of the diffuser

3) Calculate Mach number at regions within the diffuser based on schlieren images and pressure information

4) Observe shock patterns in the modeled lasing cavity

This thesis is organized to allow the reader to understand why certain design decisions were made to create the first test facility for the SBL IFX and what procedures and equipment were used throughout the experimentation. The Theory chapter provides

the crucial technical knowledge of compressible gas behavior, fluid boundary layers, and turbulent compressible jets, which will occur in the environment necessary for proper lasing to be achieved. Furthermore, the key equations used to arrive at particular conclusions have been included.

The Methods and Materials chapter explains how one could duplicate the experiment to achieve the same results. Furthermore, discussion takes place as to why certain procedures were taken.

The Results chapter provides a detailed and systematic presentation of what data was collected throughout the experimental process.

Lastly, a Conclusions and Recommendations chapter summarily explains the relevance and applications for the findings documented in this study. Additionally, this chapter will guide future endeavors in this work to achieve more accurate or noteworthy results by offering a few lessons learned.

2. Theory

2.1 Compressible Gas Dynamics

Mass flow rate can be calculated by stagnation intrinsic fluid properties using isentropic pressure and temperature relationships and conservation of mass. This results in an expression that can readily be utilized in a supersonic nozzle throat,

$$\dot{m} = \frac{p_t}{\sqrt{RT_t}} A\sqrt{\gamma}\left(1 + \frac{\gamma-1}{2}M^2\right)^{\frac{\gamma+1}{2-2\gamma}} \tag{1}$$

where the Mach number is known to be unity (8:46).

Additionally, the local Mach number in a compressible fluid can be determined once again using the conservation of mass equation and the ideal gas relationship. Only the static properties of the fluid at an instant in time and the cross-sectional area through which the fluid pass are required to determine the instantaneous Mach number,

$$M = \frac{\dot{m}RT}{pAa} \tag{2}$$

where a is the speed of sound and represented as $\sqrt{\gamma RT}$ for a perfect gas.

The pressure relationship and the critical area ratio for isentropic flow are expressed in terms of the local Mach number:

$$\frac{p_t}{p} = (1 + \frac{\gamma-1}{2}M^2)^{\frac{\gamma}{\gamma-1}} \tag{3}$$

$$\frac{A}{A^*} = \frac{\sqrt{\gamma}\left(\frac{\gamma+1}{2}\right)^{\frac{\gamma+1}{2-2\gamma}}}{M\sqrt{\gamma}\left(1+\frac{\gamma-1}{2}M^2\right)^{\frac{\gamma+1}{2-2\gamma}}} \tag{4}$$

Both results are tabulated for a wide range of Mach numbers and well published.

Equation (3) dictates the operation of velocity measurement instruments, such as a pitot-static tube. If total pressure and static pressure measurements are taken at the same location in the flow, then Mach number can be calculated.

A shock process is a radical change in measurable fluid properties such as density, temperature, and pressure. Supersonic flow rapidly adjusts to the presence of an object in the flow by means of a shock process, whereas, subsonic flow gradually adjusts the flow properties (8:33). The shock process is irreversible and adiabatic. The pressure and temperature rise across a normal shock wave can be expressed in terms of the upstream Mach number (2:7):

$$\frac{p_2}{p_1} = \frac{2\gamma M_1^2 - (\gamma-1)}{\gamma+1} \tag{5}$$

$$\frac{T_2}{T_1} = \frac{\left[2\gamma M_1^2 - (\gamma-1)\right]\left[(\gamma-1)M_1^2 + 2\right]}{(\gamma+1)^2 M_1^2} \tag{6}$$

If a fluid passes across a stationary shock wave, the fluid's static pressure will rise as dictated by equation (5). For an adiabatic process, stagnation pressure is representative of the available energy in the flow. An increase in entropy results in a dissipation of energy and, consequently, a reduction of the stagnation pressure.

The stronger the shock system the larger the stagnation pressure losses and the larger the reduction in Mach number. A normal shock wave is perpendicular to the fluid

flow. An oblique shock is inclined at an angle to the flow. Only the normal components of the flow are utilized when determining the properties across an oblique shock wave. Therefore, a normal shock will have a greater influence on the flow properties than an oblique shock, all things being equal.

Internal pipe flow experiences friction as the fluid travels down the piping. The friction of the fluid against the pipe wall influences the thermodynamic properties of the fluid. A Fanno line is a locus of possible thermodynamic states attainable by the fluid for a constant mass flux assuming steady, one-dimensional flow (17:246). The Fanno line for a given fluid, dictates that the velocity of the internal flow has limits. For subsonic flow, the fluid will gradually accelerate to a maximum of Mach 1, and the flow will become choked. Conversely, for supersonic internal flow, the fluid will decelerate to a minimum of Mach 1. The length of pipe required to choke the flow is referred to as the critical length of pipe. Fanno flow analysis is one-dimensional, and is useful for predicting changes in Mach number due to friction in constant area ducts.

2.2 Boundary Layers

As a fluid travels down the length of a surface a boundary layer develops. A boundary layer is a result of viscous forces acting on the fluid induced by a surface. These viscous forces retard the fluid velocity resulting in a velocity gradient near the wall. A momentum transfer occurs between the faster moving layers of fluid to the slower layer near the wall, which is manifested as a stress proportional to the velocity gradient (16:5).

Considering the flow over a flat-plate, Prandtl's steady flow boundary layer equations, simplified from the original Navier-Stokes equations, are:

$$u\frac{\partial u}{\partial x}+v\frac{\partial u}{\partial y}=-\frac{1}{\rho}\frac{dp}{dx}+v\frac{\partial^2 u}{\partial y^2}\tag{7}$$

$$\frac{\partial u}{\partial x}+\frac{\partial v}{\partial y}=0\tag{8}$$

where dp/dx is the pressure gradient of the fluid flow. Assuming there is a no-slip boundary condition at the wall (y=0) and no wall suction or blowing, then u=v=0. This simplifies equations (7) and (8) to the following form:

$$\mu\left(\frac{\partial^2 u}{\partial y^2}\right)_{y=0}=\frac{dp}{dx}\tag{9}$$

The second derivative of the boundary layer velocity profile indicates its curvature. When the second derivative equals zero a change in the concavity of the curve occurs and a point of inflection exists. This point inflection is an indicator for possible boundary layer separation (12:123).

Physically, boundary layer separation occurs when some of the retarding fluid in the boundary layer is transported into the main stream. Regions of adverse pressure gradients impede the fluid velocity due to the small kinetic energy that exists in the boundary layer. Ultimately, the flow reverses its direction and pulls away from the surface that it was traveling along. The point where the flow reverses direction is called the separation point. Once separation has taken place, the static pressure along the surface generating the boundary layer decreases dramatically. Furthermore, a decrease in the available energy in the flow takes place at the expense of kinetic energy.

The Reynolds number is one of fluid dynamics most familiar non-dimensional parameters and is a key in understanding the behavior of boundary layers. Reynolds number is defined for internal pipe flow in equation (10)

$$\mathrm{Re}_D = \frac{\rho V D}{\mu} \tag{10}$$

where D is the diameter of the pipe. Reynolds number is a ratio of a fluid's kinetic to viscous energy. The more kinetic energy a fluid has, the more likely it will overcome adverse pressure gradients.

2.3 Compressible Turbulent Jets

An incompressible jet firing into a quiescent environment creates the well-understood structure shown in Figure 2.1. The potential core can be approximated as laminar flow that extends outward from the nozzle exit plane a distance of five nozzle widths. The potential core is between mixing layers that separate the fast moving jet with the quiescent external flow creating turbulence if the Reynolds number is high enough (9:166). These mixing layers extend in width as the flow moves further downstream.
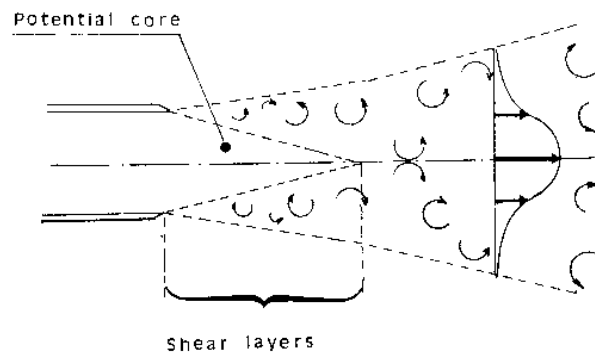
Figure 2.1 Basic Components of a Turbulent Jet (9:166)

A compressible jet consists of the same basic structures of a potential core and mixing layers, but with the added features of varying temperature and viscosity.

Furthermore, shock waves and expansion fans may be contained within the jet as dictated by the external flow pressure conditions. The propagation of a turbulent jet into any medium is characterized by, among other factors, temperature. In a compressible jet, stagnation temperatures are redistributed in part due to the non-uniform intensity of heat and momentum transfer. Consequently, a fundamental difference between an incompressible and compressible jet is the manner in which it propagates downstream of the nozzle (1:259). The propagation of the jet can vary in shear layer width and distance traveled before completely mixing into the surrounding environment.

The nozzle exit plane and external flow pressures are crucial properties in understanding the behavior of a compressible jet. When the pressure of a fluid exuding from a nozzle matches the surrounding environment, the nozzle is operating on-design and the fluid is perfectly expanded. At these pressure conditions, no shock wave or expansion waves exist within the jet. If a nozzle is operating off-design, it may be overexpanded or underexpanded. In the underexpanded case, the fluid pressure at the nozzle exit plane is greater than the ambient pressure. As a result, within the free jet, expansion waves form to further reduce the pressure to ambient conditions.
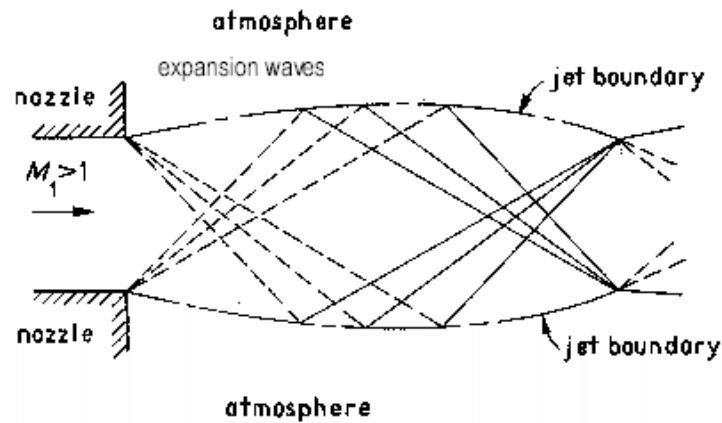
Figure 2.2 Underexpanded Jet (10:42)

Figure 2.2 demonstrates this phenomenon. Downstream, the flow is gradually turned into itself producing compression waves. Lastly, expansion waves form to complete the latticework of disturbances within the free jet that are known as "shock diamonds".

Conversely, an overexpanded nozzle fluid flow occurs when the fluid pressure at the nozzle exit plane is below ambient conditions.
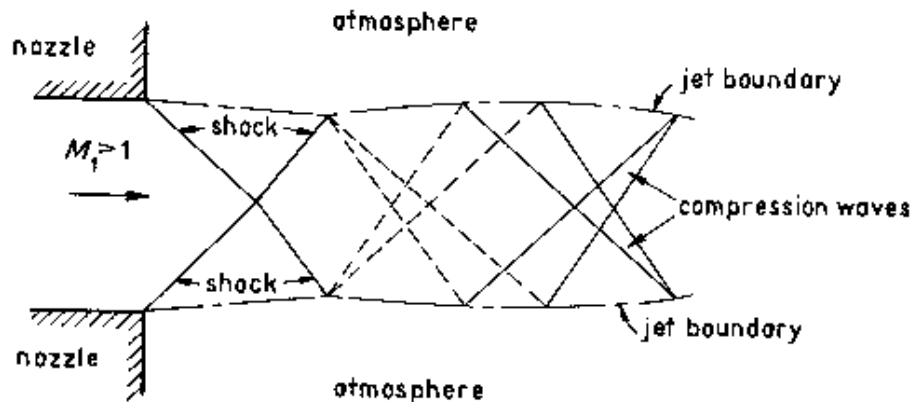
Figure 2.3 Diamond Pattern Formed in Overexpanded Jet (10:43)

Consequently, shock waves form immediately downstream of the exit plane, as seen in Figure 2.3. These shock waves compress the fluid and thereby equalize the jet pressure

2-7

to the ambient pressure. The same diamond-pattern forms within the overexpanded jet as the fluid is turned away from and into itself. In an underexpanded jet, the expansion fans forming immediately downstream of the nozzle exit plane cause the boundary of the free jet to bow outward as the flow is turned outward. Whereas, in an overexpanded jet, the jet boundary initially turns inward due to the shock wave formation seen in Figure 2.3. Therefore, a two-dimensional, planar, underexpanded free jet is wider than the free jet formed for the overexpanded condition.
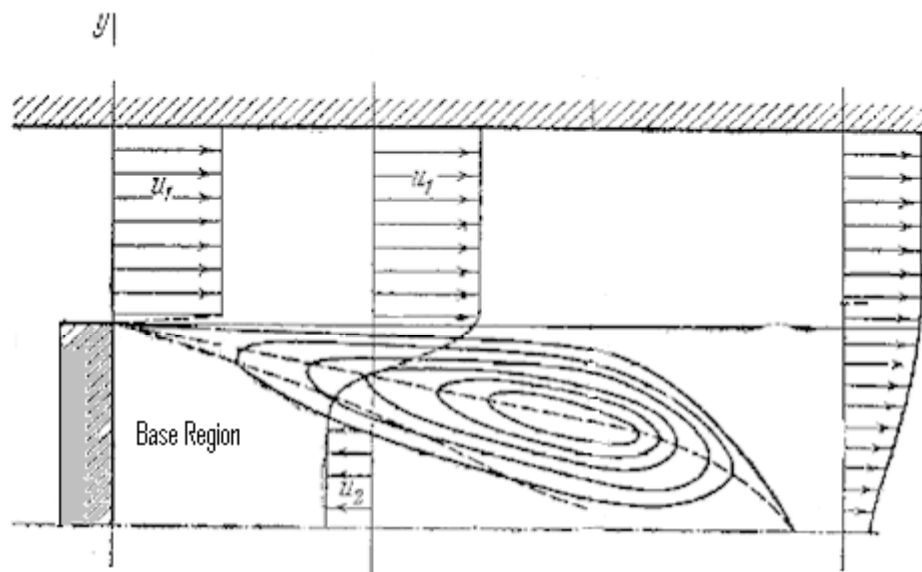
Figure 2.4 Circulation Zone at Base Region (1:391)

The base of a nozzle is referred to as the base region and is an area of complex fluid flow. As flow leaves a nozzle, the mixing layers entrain the quiescent fluid, which results in circulation around the base of the nozzle and is depicted in Figure 2.4. The circulating fluid could impinge the nozzle base and result in an increased stagnation pressure at the base region. The influence circulation zones have on pressure near a nozzle base is of concern with supersonic, nozzle arrays.

2-8

Nozzle clusters or arrays are groupings of nozzles in close proximity to each

other. The jets they form may interact with each other creating a complex flow field of

interacting shear layers, compression and expansion waves, and turbulent mixing.

Furthermore, as the nozzles operate at various ambient pressures, the jet interaction

changes with the changing flow structures.
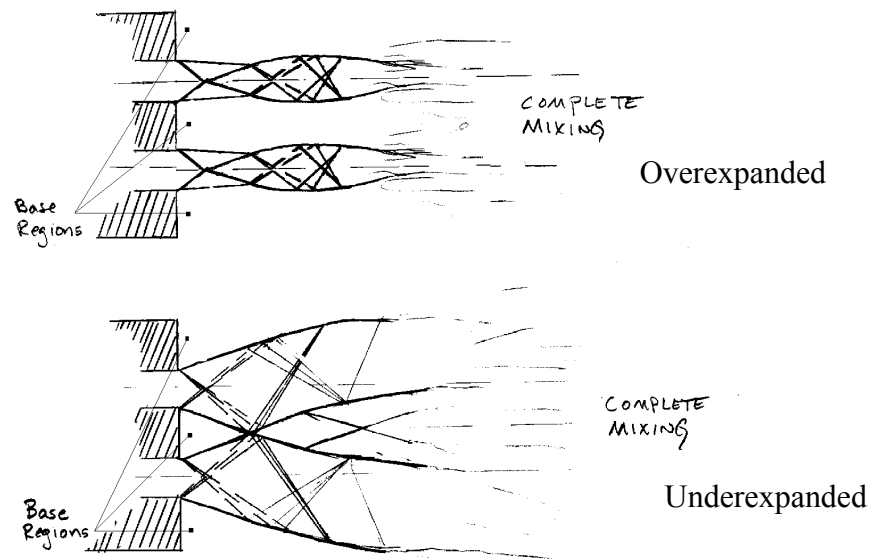
Figure 2.5 A Nozzle Cluster Operating Off-Design (5: 24)

Figure 2.5 demonstrates the two possible off-design jet interactions. If the jets are

overexpanded, little interaction occurs. However, when the clustered jets are

underexpanded, the jet plumes are wider than when the jets are overexpanded. The width

of the jets causes the fluid of the individual jets to intersect with one another. In the

underexpanded case, a small cavity between the two jets form at the nozzle base that is

isolated from the pressure further downstream, and as a result, the pressure within this

cavity is only a function of the circulation described earlier around base regions. If the

base pressure within this cavity increases with time and surpasses the nozzle exit

pressure, the jets will compensate and shift from an underexpanded jet to an overexpanded jet. The nozzle base pressure within the isolated cavity has been experimentally proven to be considerably larger than the ambient pressure (5:28). Once the jets become overexpanded, the jet plumes narrow and expose the isolated cavity at the nozzle base to the ambient pressure, and relieve the region of the higher pressure.

Another characteristic of nozzle clusters is that overexpanded clusters of jets diffuse into the surrounding fluid in a much shorter distance than underexpanded clusters. From experiments performed by Bjurstrom, the distance downstream that an overexpanded cluster of jets propagated before completely mixing into the surrounding fluid never exceeded seven nozzle widths for a range of ambient fluid pressures (5:24). Whereas, underexpanded clusters with the same nozzle-to-base ratio propagated downstream as far as 15 nozzle widths downstream. These tests were performed with various nozzle clusters and the nozzle-to-base width ratio was 0.5-4.

2.4 Loss Calculations

Fluid traveling through a pipe experiences irreversible transformations in mechanical energy to thermal energy due to friction and heat transfer. This loss in mechanical energy is called head loss and is derived from the energy equation:

$$h_l = \frac{\Delta p}{\rho} \tag{11}$$

assuming the pipe is of constant cross-section and neglecting gravity. Head loss has dimensions of energy per unit mass, or equivalently length squared per time squared. For turbulent flow, the change in pressure term can be shown to be a function of pipe

diameter, length, roughness, average flow velocity, fluid density, and viscosity (6:366).

Consequently, head loss can be reformulated as:

$$h_l = f \frac{L}{D} \frac{\bar{V}^2}{2}$$ (12)

where the Darcy friction factor is found experimentally and graphically displayed in the well-known Moody plot (6:349).

Further losses in pipes exist when a fluid passes through bends or abrupt area changes, which can result in flow separation. Through pipe bends, these losses are commonly expressed using an equivalent length:

$$h_l = f \frac{L_e}{D} \frac{\bar{V}^2}{2}$$ (13)

which can be found in various mechanical engineering handbooks (6:353). The preferred loss formula for sudden expansions or contractions is:

$$h_l = K \frac{\bar{V}^2}{2}$$ (14)

where the loss coefficient, K can also be found in the literature (6:353).

2.5 Supersonic Diffuser Theory

A supersonic diffuser has a throat that is prone to choking if designed incorrectly. A throat becomes choked if the mass flow through a given area has reached a maximum. In the case of a convergent area, when the flow becomes choked, the Mach number will become unity. The design of a diffuser throat is complex due to a starting condition that is not fully understood (4:173). At the startup of a supersonic wind tunnel, the working fluid is accelerated creating a normal shock wave, which propagates down the length of

the test section and subsequent diffuser. The diffuser throat must be large enough to "swallow" this initial transient shock wave. The minimum diffuser throat area is a function of the total pressure ratio across a normal shock wave created by the maximum Mach number in the test section and formulated as:

$$\frac{A_{throat2}}{A_{throat1}} = \frac{p_{t1}}{p_{t2}}$$ (15)

where throat 2 refers to the diffuser throat and throat 1 is the nozzle throat (13:144). If the diffuser throat is smaller than the required starting value and the transient normal shock cannot be "swallowed", the diffuser unstarts and the normal shock remains upstream of the diffuser (4:173). If a supersonic diffuser unstarts when applied to a supersonic wind tunnel, the flow throughout the test section will become subsonic.

If operating properly and the fluid settles to a steady state as a result of the normal shock moving out of the system, the diffuser throat takes on a different value than that calculated in equation (15). Sizing the diffuser throat after the transient condition is well described by Anderson (4:171-174).

3. Materials and Method

3.1 Wind Tunnel Apparatus

To achieve the necessary flow through the designed test section, the AFIT High-Speed Aerodynamics, Heat-Transfer, and Fluid Flow Research Facility was used. A blow-down/vacuum combination wind tunnel capable of delivering well over 0.3 kg/s of air was used. The wind tunnel system consisting of a compressed air, a pressure regulating system, and a vacuum system can be seen schematically in Figure 3.1.
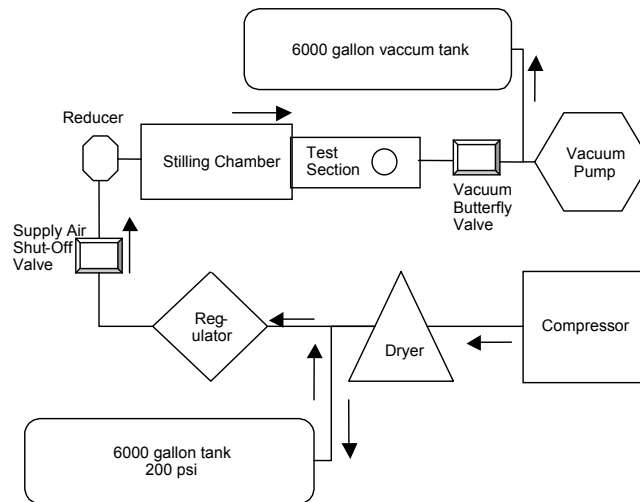
Figure 3.1 Wind Tunnel Circuit #1

3.1.1 Compressed Air System

Two Ingersoll-Rand SSR HXP 50 SE air compressors produced pressurized air to as much as 1.38 MPa (200 psi). The compressed air left the compressor pumps and entered a series of Ingersoll-Rand heatless air dryers that alternately cycled air through two desiccant beds to provide continuous flow. A 22.7-m^3 (6000-gallon) supply tank was filled and pressurized to the same pressure as the compressor air.

3.1.2 Pressure Regulation

The air in the 22.7-m^3 (6000-gallon) tank at 1.38 MPa (200 psi) was regulated

down to 0.62 MPa (90 psi) with a diaphragm-type pressure regulator. The pressure was

stepped down again with a 51-mm (2-in), air-loaded, pressure-reducing valve. The

reducing valve operated via a pressure difference across a diaphragm and established a

commanded pressure reduction setting by means of a manual feedback control. The

reducing pressure range was 83 kPa-0.9 MPa (12-133 psia). The reduction pressure

setting is commanded via a small precision regulator with analog gauge that allowed for

simple adjustments to be made by the operator. The supply air enters the test section via

a shut-off valve that was opened and closed by a switch located near the operator.

The stilling chamber was a 0.3-m (12-in) diameter reservoir upstream of the test

section. The chamber served the purpose of providing a reservoir of air at near stagnation

conditions. A flow straightener was build into the downstream end of the chamber.

3.1.3 Vacuum System

The vacuum required to operate the wind tunnel was provided by one 22.7-m^3

(6000-gallon) storage tank evacuated by a Stokes Model 412 MBX two stage-pumping

unit consisting of a Stokes Model 412-11 Microvac Pump. A 10-HP motor drove the

Microvac Pump and a 20-HP motor drove the first stage blower. Between wind tunnel

runs, the storage tank and vacuum lines could be evacuated within twenty minutes down

to a minimum pressure of 3 torr (0.06 psia). The mechanism used to subject the test

section to the vacuum was a slow action pneumatic butterfly valve, which could be

opened and closed by a switch conveniently located near the operator. The vacuum line

from the test section to the vacuum tank was 19.05-cm (7.5- in) in diameter and 22.25 meters (73 feet) long. Six 90-degree and two 45-degree elbows existed in the line.

3.1.4 Modified Wind Tunnel Circuit

A second wind tunnel circuit was also used to perform testing. A schematic of the modified wind tunnel circuit is shown in Figure 3.2. The supply air system was removed from the loop, and a 5-cm ball valve was attached to the upstream end of the stilling chamber.
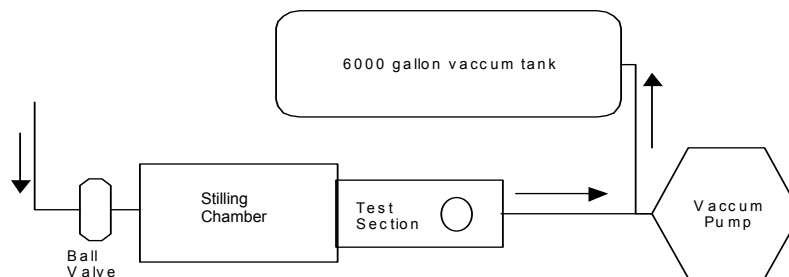
Figure 3.2 Wind Tunnel Circuit #2

This allowed the pressure in the stilling chamber to be regulated manually with the ball valve handle. Once the entire system up to the ball valve was evacuated of air, the ball valve was opened allowing air to rush into the test section providing the necessary run conditions. The amount the ball valve was opened dictated the stilling chamber pressure. Using the ball valve, the range of pressures within the stilling chamber ranged from 0-86 kPa (0-12.5 psia).

3.2 Test Section Design

Figure 3.3 is a two-dimensional schematic of one quadrant of the SBL IFX. The major components are the nozzle array, lasing cavity, diffuser, and centerbody. The entire

structure is over 6-m long and 2-m high. Therefore, each component must be scaled and adapted to the AFIT wind tunnel facility.
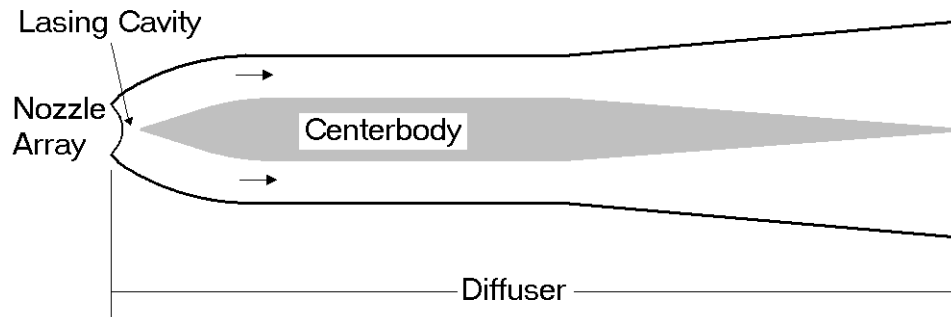
Figure 3.3 One Quadrant of SBL IFX

The criteria for building the test section were set forward by both the United States Air Force SBL IFX program office and TRW, Inc. The following is a list of the necessary design criteria:

1.) Model one quadrant or 90 deg arc of the SBL IFX nozzle stack and Exhaust Manifold Assembly (or "diffuser" for simplicity)

2.) Ensure the flow leaving the nozzle exit plane is greater than Mach 1.2

3.) Build a ten-nozzle array consisting of nine full nozzles and a half nozzle on each end of the array

4.) Ensure the nozzles have a half angle near 15 deg

3.2.1 Scale

The first step in the design process was to determine the model scale that would best suit the testing facility and flow conditions. The model needed to be small so Reynolds numbers between the real and simulated flow were close. However, the nozzle throats needed to be large enough to avoid viscous effects that would retard the flow and

prevent supersonic speeds. Furthermore, the length of the test section was limited by the physical space available in the test facility. A 1/5th scale of all components in Figure 3.3 was deemed the best compromise amongst all concerns.

3.2.2 Nozzle Array

The computer-generated model shown in Figure 3.4 is a 1/5th scale nozzle array with hardware attachment points. The width across all ten nozzles is 6.58 cm (2.59 in), and dictates the width of the entire test section.
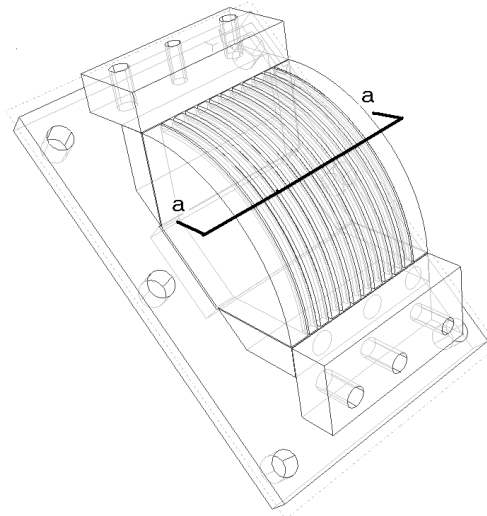
Figure 3.4 Isometric View of Nozzle Array

For a 1/5th scale model, a single nozzle throat is 1-mm (0.039-in), and the throat area of all ten nozzles is 4.36 cm^2 (1.716 in^2). A sketch of the nozzle array cross-section is shown in Figure 3.5 and dimensions in Table 3.1. The diverging portion of the nozzle was machined to ensure a 15 deg nozzle half angle. The angle of the converging section of the nozzle was chosen to be 10 deg.
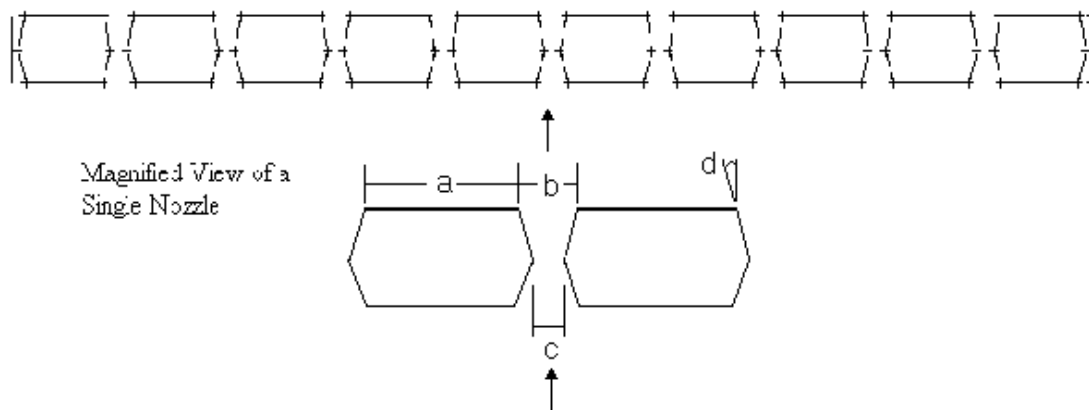
Figure 3.5 Cross-Section of Nozzle Array (Section a-a)

Table 3.1 Dimensions for a Single Nozzle in Array

	Nomenclature	*Dimension*
a	Base	4.6 mm (0.181 in)
b	Exit Width	1.98 mm (0.078 in)
c	Throat Width	1 mm (0.039 in)
d	Half-Angle	15-degrees

For manufacturing purposes, the nozzle walls were not contoured. Since no contour exists in the walls of each nozzle, some losses were expected. To design the nozzles for a particular Mach number required knowledge of how much of a loss was expected. From preliminary tests, described in Appendix A, the Mach number produced from a nozzle without contoured walls is approximately 15% less than that expected if the nozzle were designed for isentropic expansion. This was the baseline to determine the expansion ratio required to achieve one of the design criteria of a Mach number greater than 1.2 at the exit plane of the nozzle array.

The fundamental differences in the scaled nozzle array from the design created by TRW, Inc. were the lack of injected flow in the diverging section of the nozzle, no wall contour to prevent losses, and a much smaller expansion ratio. Although these differences existed, similarity between the two designs (principally similar Mach numbers) at the nozzle exit plane was the goal. Figure 3.6 is a photograph of the completed nozzle array.
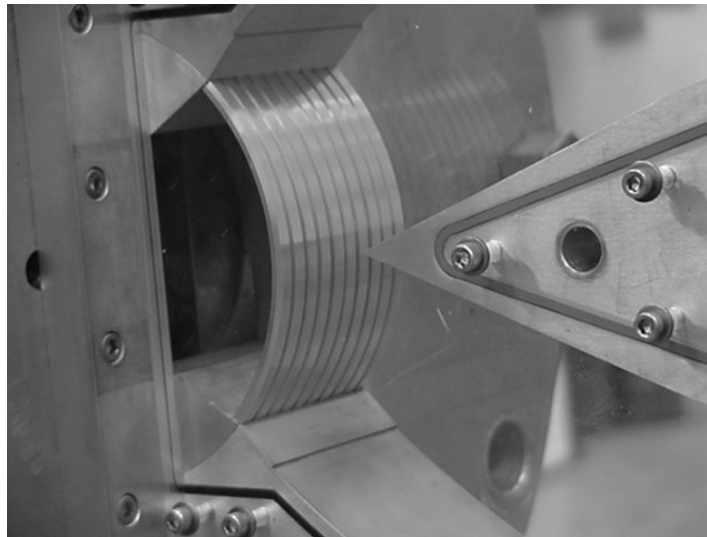
Figure 3.6 Completed Model of Nozzle Array

3.2.3 Diffuser

TRW provided the contour of the top and bottom of the diffuser. The length of the diffuser is 1.41 m (55.6 in) and the top and bottom of the diffuser were machined in three pieces. These three pieces can be viewed in Appendix B and consist of a contoured segment designed to turn the flow from a radial direction to a horizontal flow with minimal losses, and two straight segments. The height of the diffuser ranged from 33.3-

47 cm (13.1-18.48 in). The manufacture of the diffuser in segments complimented one of the design goals of modularity to allow for replacing segments with various geometries.

The majority of the sidewalls of the diffuser were made of 4.76-mm (3/16-in) thick aluminum. This allowed for lighter weight and the structural strength needed to hold its shape while subjected to a vacuum. The first 30.5 cm of the diffuser walls were made of an optical grade Plexiglas to observe the flow in the critical contoured portion of the diffuser. This region viewed through the Plexiglas is referred to as the "optical cavity". This same region in the full-size SBL IFX is referred to as the "lasing cavity" (as seen in Figure 3.3) and is the critical portion of the diffuser where lasing occurs. Since lasing does not occur for this research using the subscale model, the nomenclature "optical cavity" was deemed most appropriate.

3.2.4 Centerbody

The centerbody was an airfoil that divided the flow into two channels. Around its centerline, the airfoil was symmetric and positioned in the center of the flow, 3.05 cm downstream of the nozzles, to equally split the mass flow. The trailing edge of the airfoil was flush with the exit plane of the diffuser. The centerbody was created in three pieces: the wedge or contoured portion, the mid-section, and the tail. The half-angle of the wedge is 21 deg. The mid-section was hollow and created using 1.91-cm (¾-in) aluminum plates. Figure 3.7 shows the shape of the centerbody. Bolt holes were machined into the metal every 5 cm to provide support points to the sidewalls of the diffuser. O-ring grooves were cut on both sides of the airfoil around the outside parameter, and the leading edge was cut to a knife-edge finish.
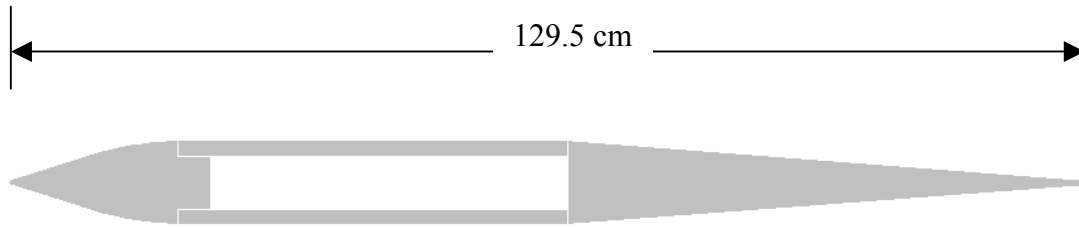
Figure 3.7 Centerbody Geometry

3.2.5 Test Section – Wind Tunnel Interface [Transition Structure]

The model diffuser needed to mate with the AFIT facility vacuum line. In an effort to balance length and weight with a gradual reduction in area to prevent radical changes in flow properties, a 76.2-cm long neck was manufactured with a declination of approximately 11 deg. This structure was referred to as the "transition structure" and is sketched in Figure 3.8.
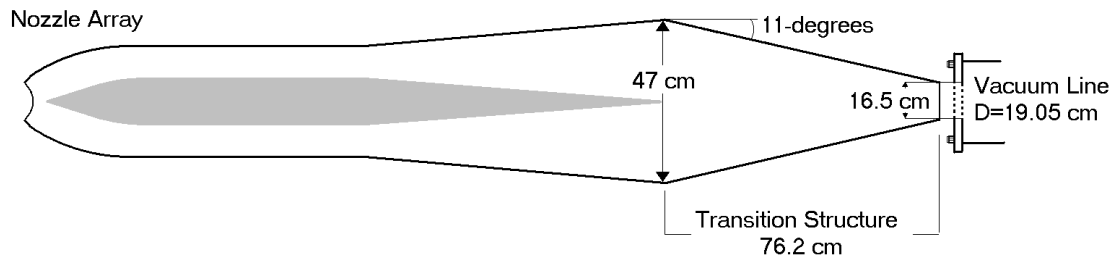
Figure 3.8 Transition Structure

Ideally, the diffuser and vacuum line would have connected without a reduction in area to restrict the flow. However, since the cross-sectional area of the diffuser was rectangular and the cross-sectional area of the vacuum line was circular, the areas could not be matched without major modifications to the facility.

After all the components were assembled, the complete and final model was formed. Figure 3.9 displays a photograph of the completed model.
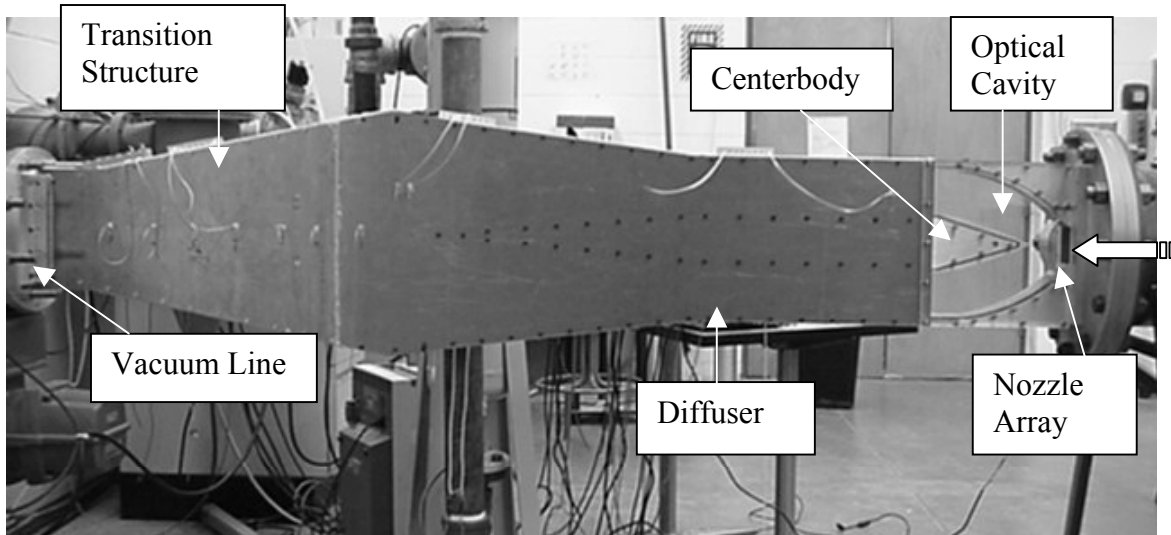
Figure 3.9 Completed Model of Diffuser and Transition Structure

3.3 Data Acquisition and Signal Conditioning

Since the fluid flow was compressible and highly unsteady, a need existed to capture many data points to analyze the fluid flow on a point-by-point bases. Therefore, the instrumentation needed to be responsive and data acquisition rapid.

3.3.1 Instrumentation

A total of seven Endevco model 8530C-50 piezoresistive pressure transducers (PTs) were used to collect information from the test section. The excitation voltage for each transducer was 10 Vdc and the range 0-50 psia. The transducer's response frequency was 40 kHz.

3.3.2 Data Acquisition System (DAS)

The Nicolet Multipro 120 Digitizer was the acquisition system of choice and interfaced with a Microsoft Windows based program run on a 386 Personal Computer.

This system consisted of four cards with 4 channels each. All flow signals were conditioned, filtered, and amplified before input to the DAS. The signals from the pressure transducers were fed to Endevco Model 4428A signal conditioners, which supplied an excitation voltage to the transducer. The sampling rate for all testing procedures was 142.7 Hz or approximately a single pressure reading every 7 ms per channel.

3.3.3 Schlieren Optical System

A schlieren system was used to observe and capture the density gradients in the optical cavity of the diffuser, and a sketch is shown in Figure 3.10.
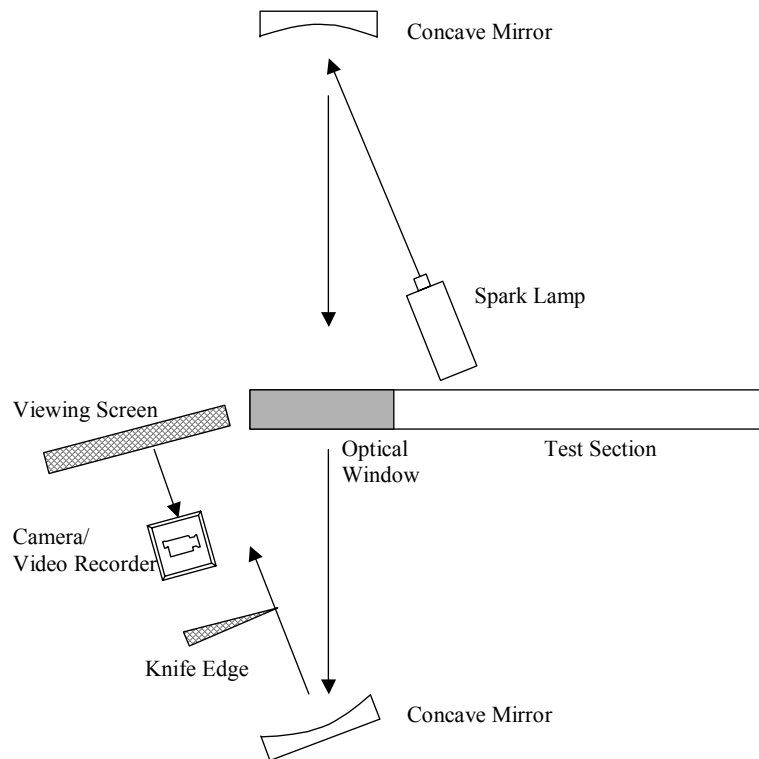
Figure 3.10 Schlieren Optical System

The viewing screen was a piece of white poster board that allowed for an undistorted image to be observed. Both digital still pictures and video of the fluid flow were

captured, which allowed for analysis and manipulation of the images. A high resolution Kodak Nikon N90s digital camera was used to collect the still images. A Sony digital video recorder allowed for quick moving shock structures to be captured and further analyzed. The video recorder shot 30 frames per second.

3.4 Experimental Procedure

Five separate test procedures (each procedure of multiple runs) took place to fully understand and explore the dynamics occurring in the test section. The schlieren optical system setup was the same for all procedures. Furthermore, the method of calibrating the pressure transducers was the same for each test. For all five procedures, a pressure transducer was located in the stilling chamber, to measure the reservoir stagnation pressure. A second transducer was located in the vacuum line 61 cm downstream of the vacuum butterfly valve, and recorded the defined "back pressure" of the system.

3.4.1 Calibration and Uncertainty

The calibration of the pressure transducers was done on the apparatus using a portable pneumatic tester. Each transducer was calibrated using two points with the pneumatic tester. All transducers were recalibrated approximately every two days to ensure accuracy.

A detailed uncertainty analysis was performed and is presented in Appendix C. For a single pressure reading, the uncertainty is +/- 0.3 psia. This uncertainty is due to bias and precision error in the pressure transducer and signal conditioner. The uncertainty in pressure readings propagates in calculations for Mach number and mass flow.

3.4.2 Wind Tunnel Operation: Circuit #1

Initially, all air valves were closed, and the electronics turned on. The schlieren spark lamp was turned on and adjustments made with the knife-edge if necessary. The butterfly valve was first switched open allowing a vacuum to be pulled on the test section, stilling chamber, and plumbing to the supply air shut-off valve. The DAS was manually triggered via a keystroke to begin the collection of data. To allow the vacuum to reach equilibrium in the test section, three seconds elapsed before any further action was taken. Next, the supply air shut-off valve was switched open allowing air to fill the stilling chamber, starting the nozzles. The supply air shut-off valve remained open until the nozzles no longer produced supersonic flow, as recognized from the schlieren image by a lack of density gradients in the lasing cavity. Throughout the run, pictures or video were taken of the viewing screen. The supply air shut-off valve was switched close. Moments later, the vacuum butterfly valve was closed. The DAS graphically displayed the collected pressure readings immediately after the vacuum butterfly valve was closed on the PC monitor via the Nicolet software.

3.4.3 Wind Tunnel Operation: Circuit #2

Initially, both the vacuum butterfly and newly installed ball valve were closed, all electronics turned on, and schlieren setup was adjusted if necessary. The butterfly valve was opened which allowed a vacuum to be pulled on the test section and stilling chamber. The DAS was manually triggered. Next in the sequence, the ball valve handle was manually turned allowing room pressure to rush into the evacuated test section. The ball valve handle could be turned to various opening settings thereby altering the reservoir pressure. Pictures were taken during the run. Once supersonic flow was no longer

produced, the vacuum butterfly valve was closed and the ball valve handle turned to close the valve.

3.4.4 Pressure Transducer Configurations and Throat Area Modifications

Three configurations were used for pressure transducer placement in the test section. Each configuration has a pressure transducer located in the stilling chamber, PT1, and downstream of the test section in the facility vacuum line, PT11. Figure 3.11 displays the location of these two transducers.
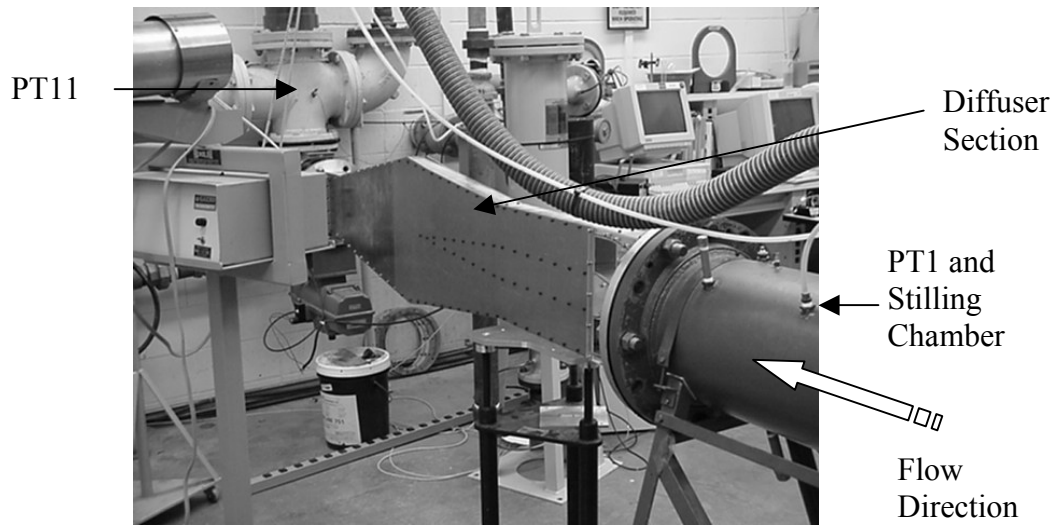
Figure 3.11 PT1 and PT11 Locations

The diffuser section pressure ports were drilled into the sidewall of one side of the diffuser. Figure 3.12 presents a schematic of configuration #1. Pressure transducers four and five are collocated. Transducer five records total pressure via a pitot tube and is the only total pressure measurement of all the three configurations.
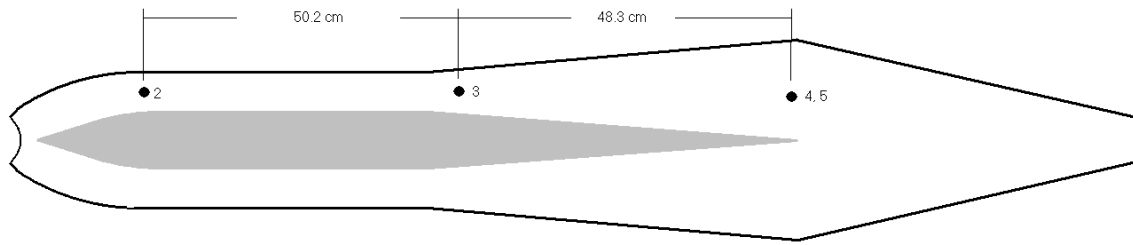
Figure 3.12 PT Configuration #1

Table 3.2 provides a list of all transducers used in configuration #1. The cross-sectional area of the diffuser at the location of each pressure port is also included. The areas listed are for a single channel made by the airfoil dissecting the flow.

Table 3.2 Cross-Sectional Areas for PT Configuration #1

Pressure Transducer (PT)	Cross-Sectional Area [cm^2 (in^2)]
1	Stilling Chamber
2	A_2 = 60.6 (9.4)
3	A_3 = 72.9 (11.3)
4	A_4 = 150.3 (23.3)
5	Pitot Tube
11	Vacuum Line

Pressure transducer configuration #2 is displayed in Figure 3.13 and associated areas in Table 3.3. All transducers have been relocated to the transition to provide detailed analysis through this region of the test section.
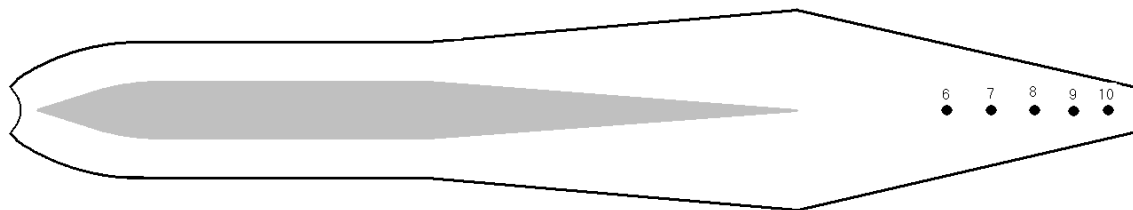
Figure 3.13 PT Configuration #2

Table 3.3 Cross-Sectional Area at Port Locations for PT Configuration #2

Pressure Transducer (PT)	Cross-Sectional Areas [cm^2 (in^2)]
1	Stilling Chamber
6	$A_6 = 258.6$ (40.1)
7	$A_7 = 238.0$ (36.9)
8	$A_8 = 204.5$ (31.7)
9	$A_9 = 183.8$ (28.5)
10	$A_{10} = 158.7$ (24.6)
11	Vacuum Line

Lastly, pressure transducer configuration #3 is displayed in Figure 3.14 and associated areas in Table 3.4. The primary difference from configuration #1 is that the transducer measuring total pressure using a pitot tube has been moved to the back of the transition, and recorded static pressure.
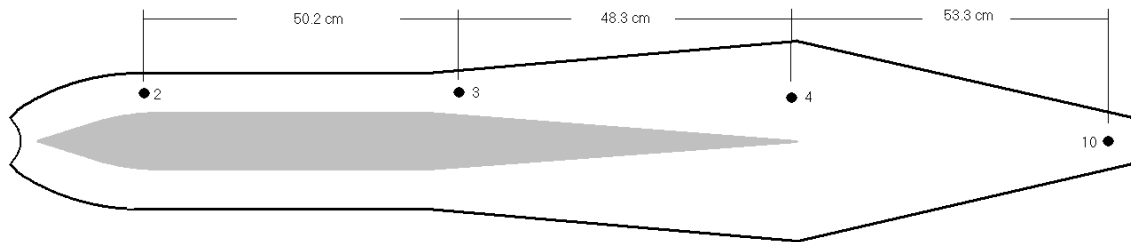
Figure 3.14 Pressure Transducer Configuration #3

Table 3.4 Cross-Sectional Areas at Pressure Port Locations for Configuration #3

Pressure Transducer (PT)	Cross-Sectional Area [cm^2 (in^2)]
1	Stilling Chamber
2	$A_2 = 60.6$ (9.4)
3	$A_3 = 72.9$ (11.3)
4	$A_4 = 150.3$ (23.3)
10	$A_{10} = 158.7$ (24.6)
11	Vacuum Line

For particular tests, nozzles were purposely obstructed. Metallic tape was cut into 15.25-cm by 0.635-cm strips. These strips were placed over 5 nozzles and arranged such that every other nozzle was blocked off. The half nozzles on each end of the array remained unobstructed. This restricted the mass flow by approximately 50% from tests when all the nozzles were unobstructed for the same reservoir pressure.

3.4.5 Test Procedure Matrix

The various combinations of pressure transducer configurations, wind tunnel operating procedures, and mass flow reduction by the obstruction of nozzles are tabulated in Table 3.5.

Table 3.5 Experimental Test Matrix

Test Procedure	Wind tunnel circuit	Pressure Transducer Configuration	Blocked Nozzles
1	1	1	No
2	1	2	No
3	1	3	Yes
4	2	2	No
5	2	3	No

4. Results

4.1 Nozzles and Diffuser

The two pressures that dictated much of the diffuser performance were the reservoir pressure seen in Figure 4.1 and the back pressure displayed in Figure 4.2 for test procedure #1.
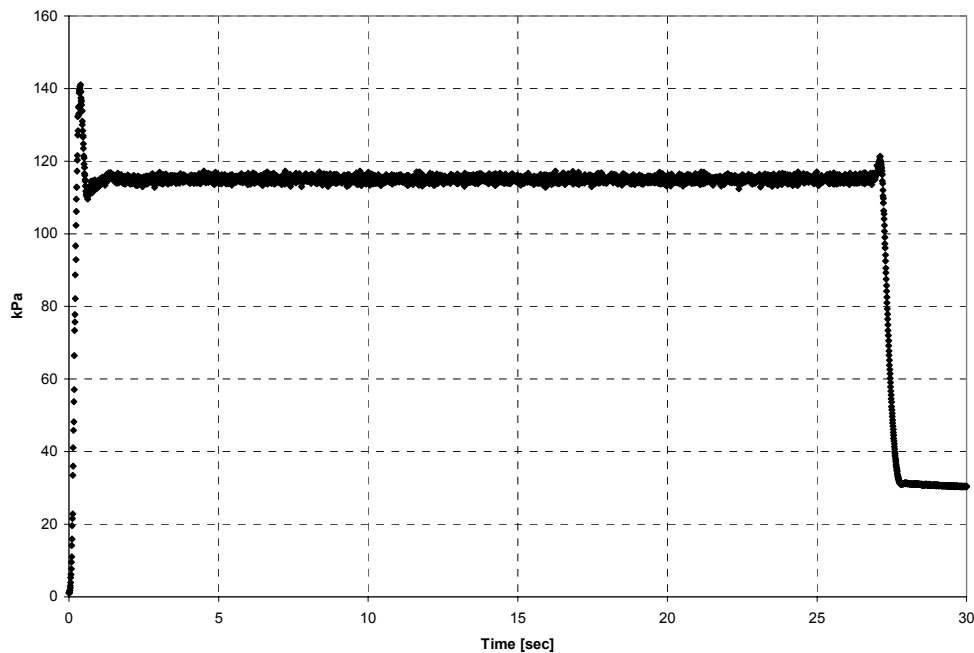
Figure 4.1 Typical Reservoir Pressure (PT1) Characteristic for Procedure #1

Although the data in Figure 4.1 and Figure 4.2 are for a single run, the same general characteristics were indicative for runs at all reservoir pressures for procedure #1. Though not shown, both Figure 4.1 and Figure 4.2 have uncertainty bands of +/- 2000 Pa (+/- 0.3 psia) with a 95% confidence level. For the specific run shown in Figure 4.1, the reservoir pressure reached consistency at 115 kPa (16 psia). After 27 seconds, the supply air shut-off valve was closed and the run ended. Figure 4.1 displays a region within the first second of the run that is transient. This is a result of the pressure reducer's

mechanical feedback loop. The time interval that displays the transient behavior varies in length and depends on the reservoir pressure. Typically, all transient behavior ends after two seconds from when the wind tunnel is started. The reservoir pressure spikes in Figure 4.1 to 145 kPa (21 psia) during this transient time interval. After the first two seconds of the run, the pressure in the stilling chamber reached a stable pressure and remained constant through the rest of the run.
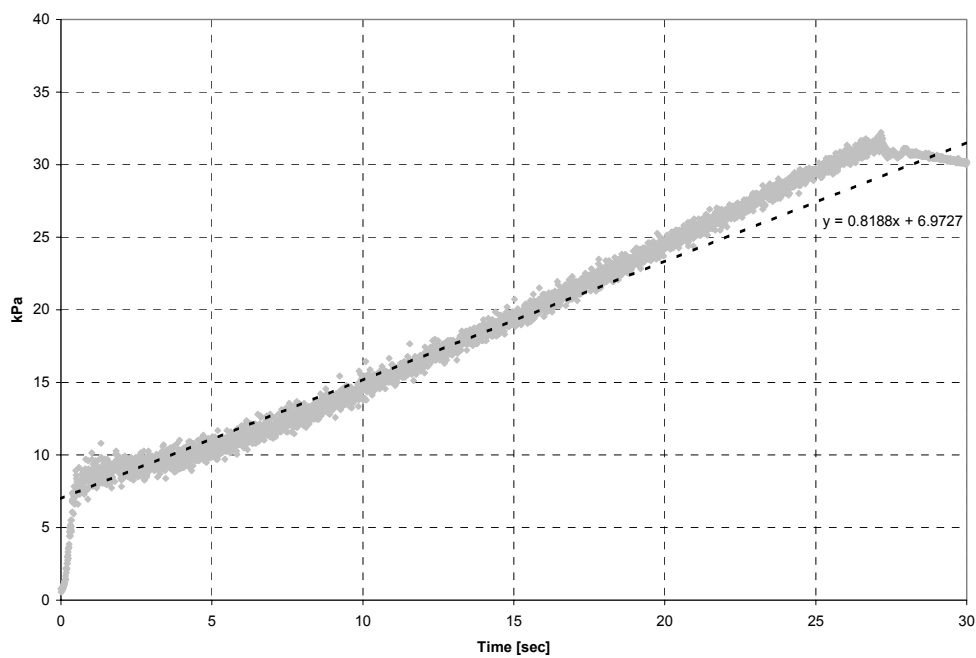
Figure 4.2 Typical Back Pressure (PT11) Characteristic for Procedure #1

Figure 4.2 provides information about the nature of the filling vacuum tank and lines. Within the transient time interval, the initial back pressure of 414 Pa (0.06 psia) jumped to 6895 Pa (1 psia). The magnitude of the jump in back pressure at PT11 during the transient time interval also varies with reservoir pressure. The rise in back pressure within the first second of the run can be attributed to head loss in the vacuum line. The head loss was analytically determined to be 3450 Pa (0.5 psia) and assumes an average

velocity and density within the vacuum lines. The detailed calculations of the head loss can be found in Appendix D.

After the transient condition, Figure 4.2 demonstrates quasi-linear properties as expected for a steady mass flow rate. From the linear regression line fit to the data in Figure 4.2, the back pressure rose at a rate of 830 Pa/s (0.12 psia/s). Analytically, the back pressure was predicted to rise at a rate of 1026 Pa/s (0.15 psi/s) as shown in Appendix E.
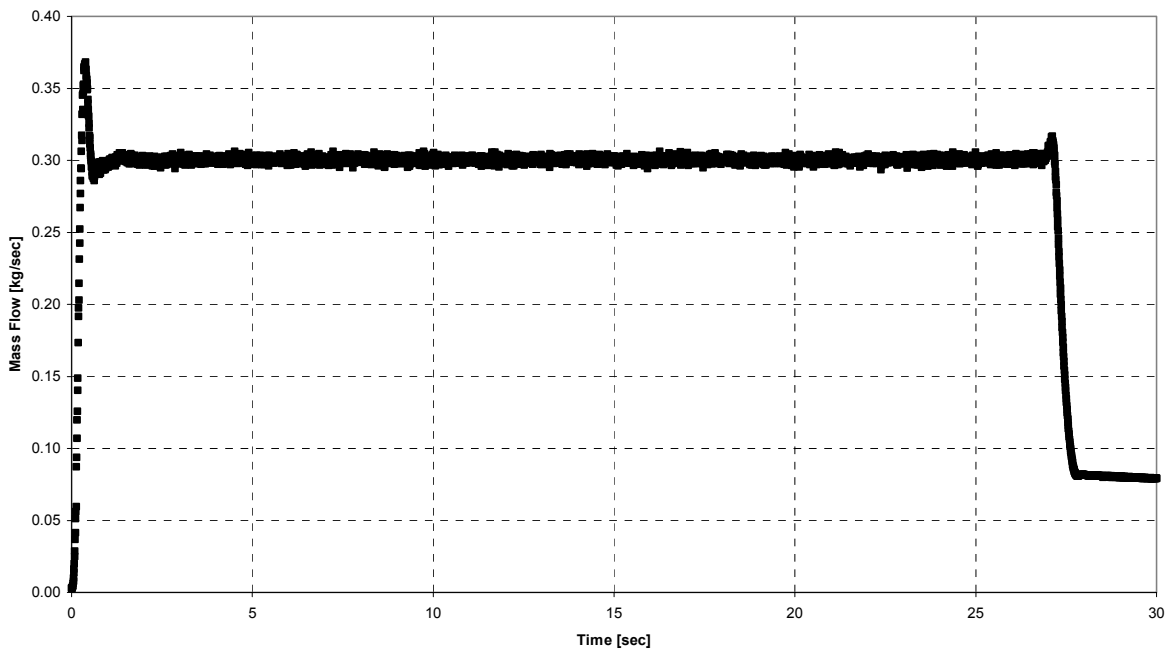
Figure 4.3 Typical Mass Flow Rate for Procedure #1

The mass flow rate was calculated based on Eq. (1) applied at the throat of the nozzle array where the Mach number is assumed to be unity at all times for all runs. The mass flow calculations that correspond to the reservoir pressure in Figure 4.1 are plotted in Figure 4.3. The shape of the curve in Figure 4.3 is the same as Figure 4.1, since mass flow is a function of the reservoir pressure and temperature, and is an example of all runs

performed using procedure #1. The temperature in the reservoir was assumed to be room

temperature (290K) and constant. The maximum error calculated in Appendix C for a

single mass flow calculation was determined to be +/- 4.7 g/sec.
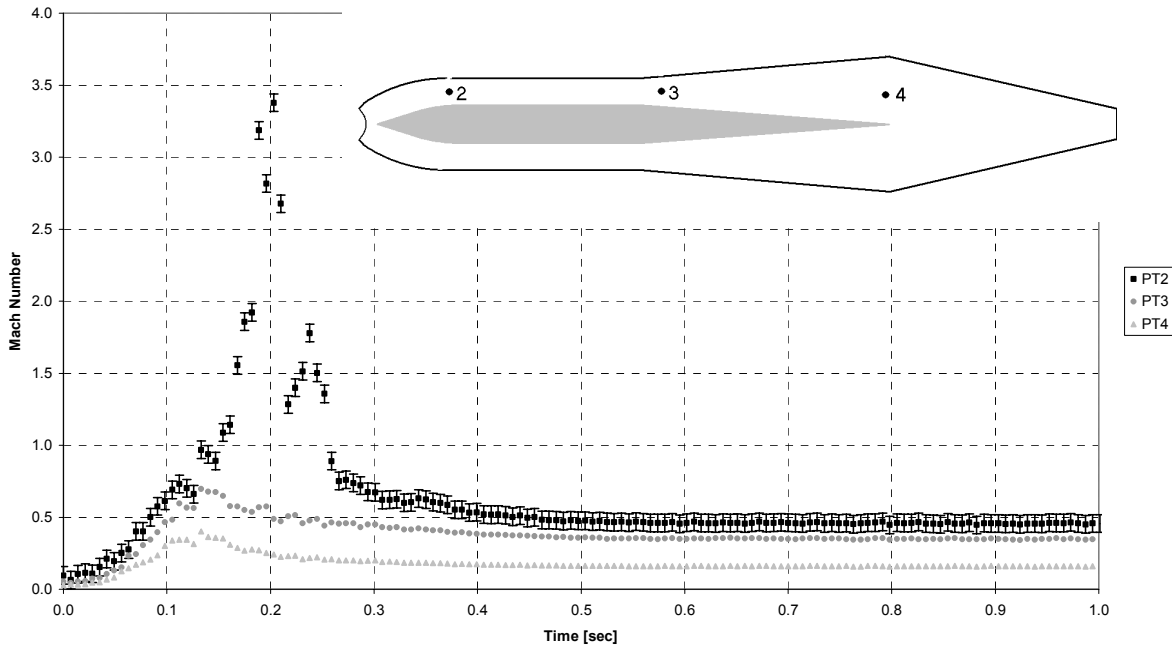
Figure 4.4 Mach Numbers for Procedure #1 During Transient Time Interval

For test procedure #1, the Mach numbers at PT2, PT3, and PT4 were calculated

for all times using static pressure and cross-sectional area as shown in Eq. (2). The

results are displayed in Figure 4.4. The maximum error of a single Mach number

calculation was determined in Appendix C to be +/- 0.1. Error bars were only placed on

data from PT2 to graphically display the error. The highest velocities were found to be at

PT2, closest to the nozzle array. As the fluid traveled down the length of the diffuser, it

slowed. Figure 4.4 shows that the fluid was subsonic at PT4 as seen in Figure 4.4 during

the transient time interval. However, a peak value of Mach 3.37 is found to occur at PT2.

The temperature used to calculate the maximum Mach number at PT2 during the

transient interval of the run was 88K and found by iteration. The iteration process to find

the temperature involved first making an initial guess of the local temperature at PT2.

The Mach number at PT2 was calculated using the temperature initially guessed and the

static pressure recorded. From isentropic relationships tabulated in ref (2) the Mach

number that corresponded to the ratio of the static-to-total temperature ratio (or the local

temperature guessed divided by the stagnation temperature in the stilling chamber) was

compared to the Mach number calculated. If the Mach number calculated using the

initial temperature guessed and the static pressure recorded did not match the tabulated

isentropic Mach number corresponding to the ratio of the local temperature guessed to

the stagnation temperature in the stilling chamber then the local temperature was

adjusted. This process was continued until the calculated Mach number converged on the

Mach number tabulated. Considering the Mach numbers at all other locations (subsonic

in value) ambient temperature was used to calculate the Mach number.

During the steady-state region of the run, the Mach numbers at PT3 and PT4 were

well predicted by the calculations made in Appendix F and within 10% of the

experimental value. Figure 4.5 displays the steady-state Mach numbers at the various

locations down the length of the diffuser.
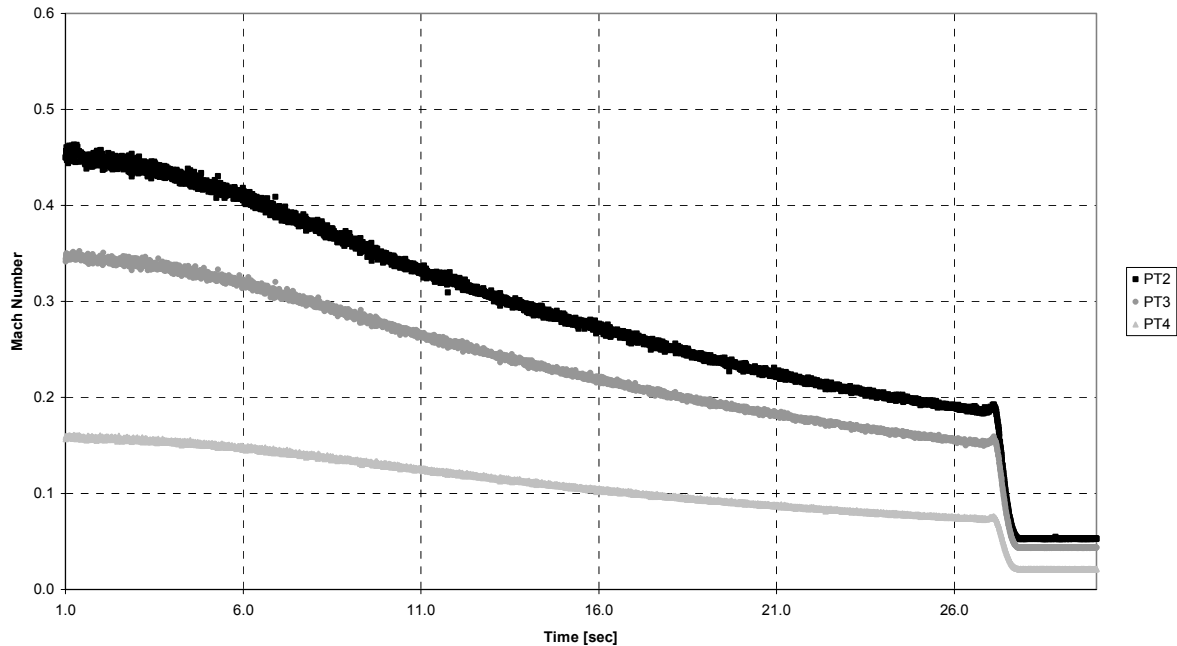
Figure 4.5 Steady-State Mach Numbers for Procedure #1

During steady-state operation, the Mach numbers at PT3 and PT4 were approximately

0.35 and below, so the fluid flow can be appropriately assumed incompressible at these

transducer locations.

The pitot tube at PT5 provided total pressure loss information when compared to

the reservoir pressure. Figure 4.6 graphically demonstrates the reduction in total pressure

as the flow travels down the diffuser. Losses due to shock waves and friction are higher

at higher Mach numbers; therefore, the larger total losses would be expected in the

beginning of the run. From Figure 4.6, the largest difference in total pressures occurs in

the first five seconds of the run, when the Mach numbers at all transducer locations were

highest.
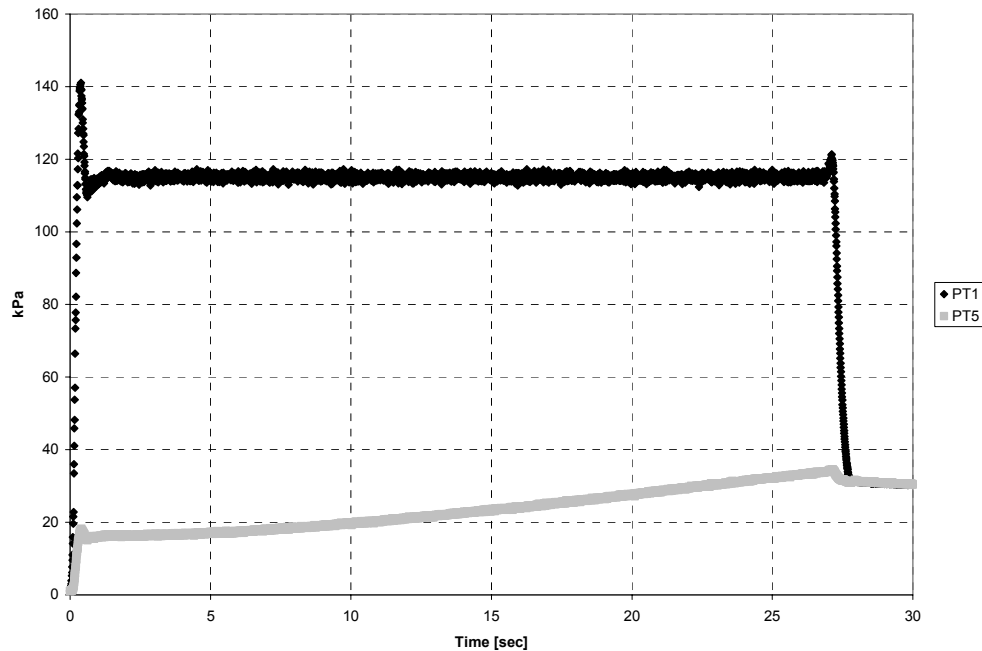
Figure 4.6 Total Pressure Comparison of PT1 and PT5 for Procedure #1

The schlieren optical system described in Chapter 3 makes use of both still

pictures and video. A video recorder was used to capture images during the transient

interval of the run. The video images revealed the existence of an oblique shock wave at

the first measurable time in the run, t = 0.1 seconds, initially attached to the leading edge

of the wedge. Within a tenth of a second, the oblique shock wave folded up on itself,

detached from the wedge, and stood upstream of the leading edge of the wedge. The

sequence of frames exposing the movement of the oblique shock wave is in Figure 4.7.
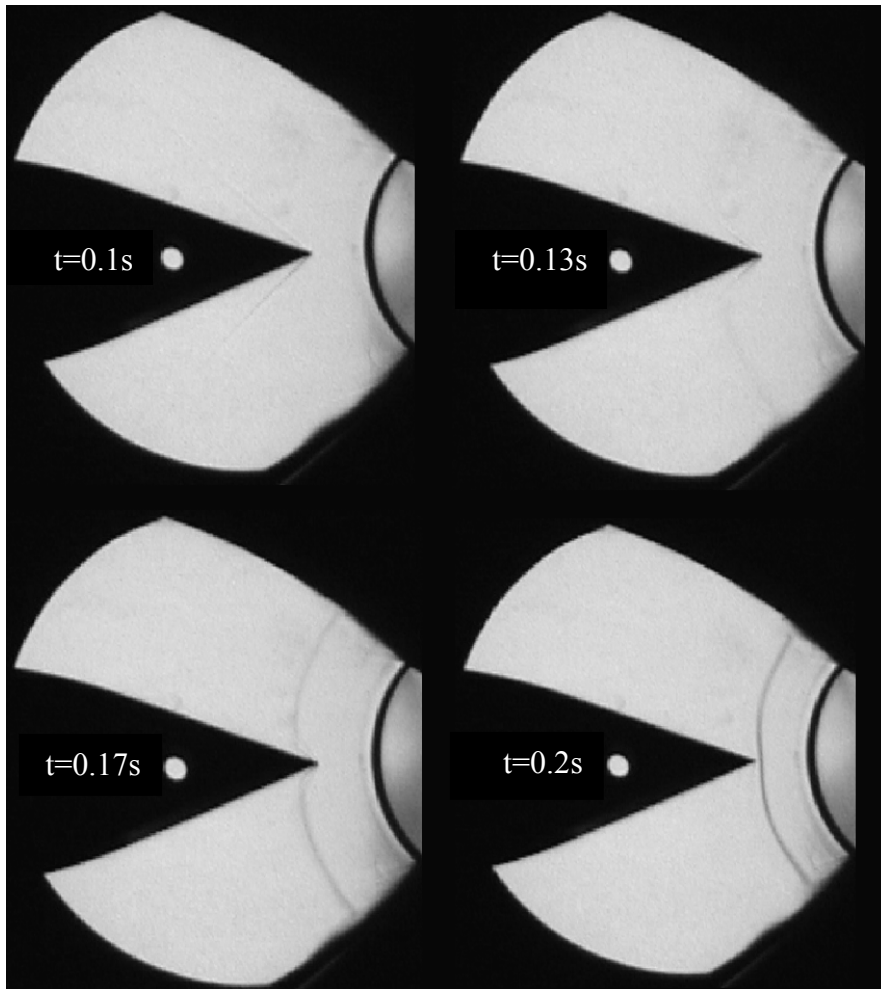
Figure 4.7 Schlieren Images of Oblique Shock Wave Motion During Procedure #1

An enlarged sequence of photographs is displayed in Appendix G. The measured shock wave angle from Figure 4.7 and the wedge half-angle dictate that the flow at the leading edge of the wedge was traveling at Mach 2.7. The nozzle exit plane Mach number was designed to be 1.9; therefore, the multiple jets must be underexpanded and ultimately accelerate the fluid to Mach 2.7 in the distance between the nozzle array and the leading edge of the centerbody.

Due to the difficulty of aligning the precise moment that the reservoir pressure at PT1 coincided with the picture displayed at t=0.1s in Figure 4.7, the calculation of a

single Reynolds number at that moment could not accomplished. So, a range of possible

Reynolds numbers was calculated to be 9×10^4 to 5×10^5. The characteristic length used

was the arc length at the leading edge of the centerbody at the radius from the center of

curvature of the nozzle array to the centerbody (the radius was 0.105 m), and was also

used by TRW. The velocity and static temperature at the wedge were determined from

the observed Mach number in Figure 4.7 at t=0.1s. The density was deduced from a

calculated static pressure at the leading edge of the centerbody based on Mach number

and the pressure at PT1.

Whether similarity has been achieved to the full-scale SBL IFX design is a

concern during the transient time interval. The computational Reynolds number at the

leading edge of the wedge determined by TRW was approximately 1.8×10^4. Therefore,

the Reynolds number at the leading edge of the wedge for the subscale model may be an

order of magnitude different than the numerical results found by TRW.
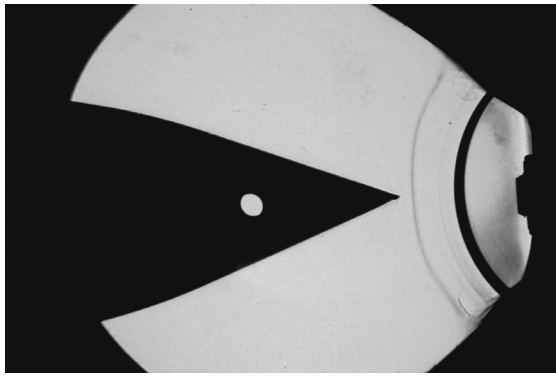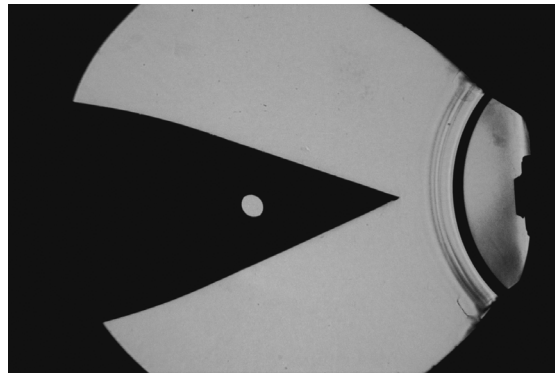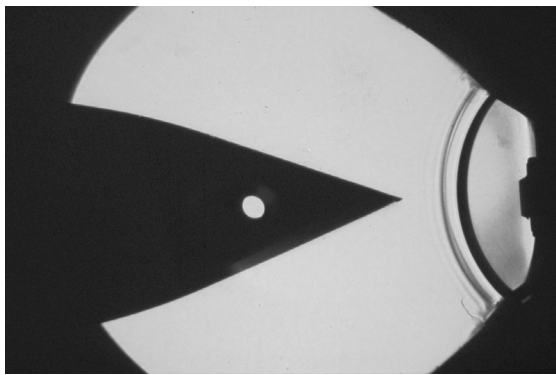
t = 5 sec	t = 10 sec
t = 15 sec	t = 20 sec
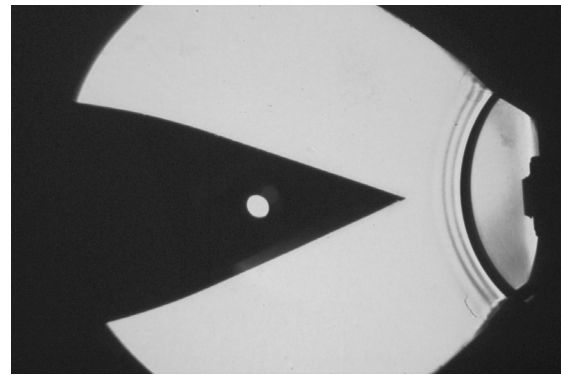
Figure 4.8 Sequence of Schlieren Photographs for Procedure #1

After the initial transient, during steady state conditions, the shock wave moved upstream

toward the nozzle array as the pressure at PT11 increased. Figure 4.8 provides a

sequence of pictures taken with the digital camera every five seconds once the flow

became steady state for procedure #1. At 5 seconds into the run, a well-defined shock

wave stood upstream of the wedge.   Five seconds later, the shock wave traveled

upstream. At 15 seconds, the shock wave moved even further upstream and appeared to

have thickened, indicating numerous waves in close proximity. Lastly, at 20 seconds,

numerous lighter colored waves appeared. Considering the radial direction of the flow as

it exits the nozzles, the shock wave was normal to the moving fluid. The images reveal

that the flow was symmetric.

Figure 4.9 is an enlarged view of the image in Figure 4.8 at t = 5 seconds. The

bottom portion of the optical window is displayed.
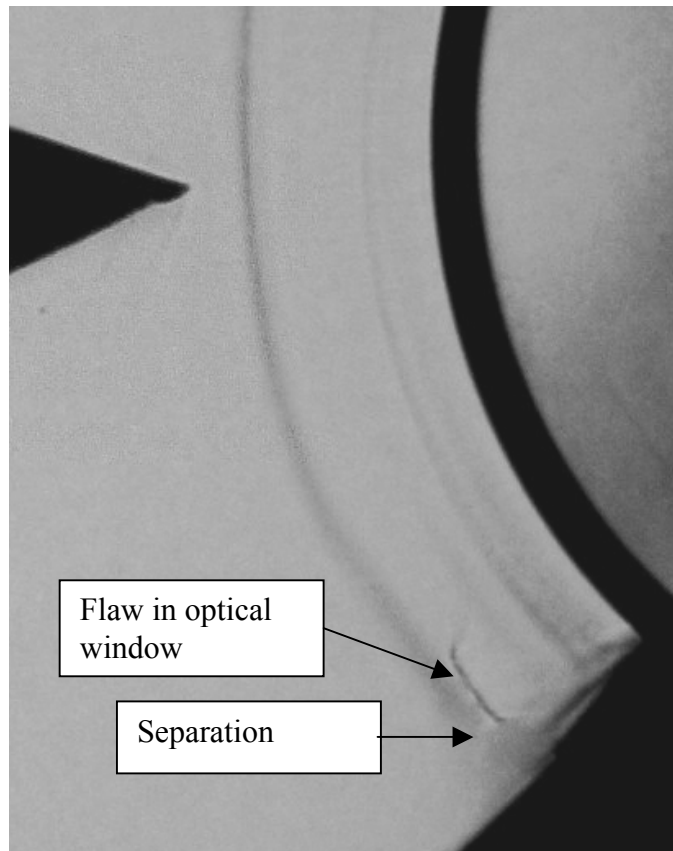
Figure 4.9 Schlieren Photo at t = 5 Seconds for Procedure #1

Between the downstream shock wave and the nozzle exit plane, numerous small

disturbances can be viewed in Figure 4.9. These faint radial waves are suspected of

being intersecting expansion and shock waves within each individual jet. The light rays

of the schlieren optical system spark lamp cross the jets in the direction shown in Figure

4.10. Due to the orientation of the nozzles and the light source, the shock diamonds

discussed in Chapter 2 are unseen. Instead, the intersecting expansion, shock, and

compression waves are the strongest density gradients in the image. They appear as lines or poles that extend perpendicular to the flow. These poles would then be the apexes of each shock diamond, and the distance between each pole is the length of a single diamond. The faint radial lines immediately downstream of the nozzle array in Figure 4.9 may be the apexes of numerous shock diamonds.

Theoretically, if the nozzles were perfectly machined and the Mach number at each exit of each nozzle were identical, then all ten jets would have these poles aligned on the viewing screen for each diamond. The image would appear as if only a single jet were present. However, as there is a +/- 0.051-mm (+/- 0.002-in) tolerance for all machined surfaces and the image is of a fluid channel 6.6-cm across, the poles are not seen as one. Rather they may be observed as blurred or thickened lines.
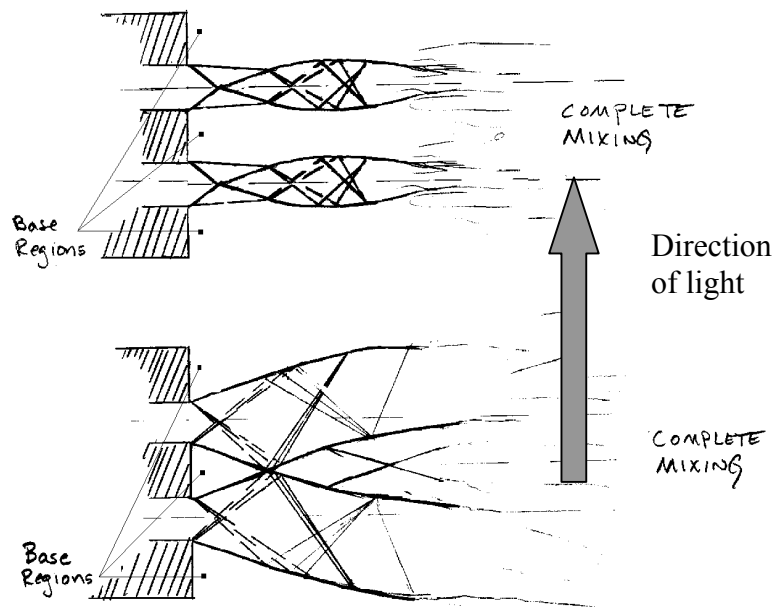
Figure 4.10 Orientation of Schlieren Light Rays in all Experimentation

If these radial waves are the apexes of shock diamonds, the distance they were observed downstream of the nozzle array can indicate whether the flow is underexpanded or overexpanded . For an underexpanded nozzle, the shock diamond pattern extends no more than 10-15 nozzle widths downstream of the nozzle exit plane (5). For an overexpanded nozzle, the distance is no more than 6-7 nozzle widths (5). The radial waves in Figure 4.9 are 7.3 nozzle widths downstream, so the jets of the nozzle array were most likely underexpanded based on observation at this time for procedure #1.

Along the bottom surface, flow interaction with the wall can be readily seen in Figure 4.9. The flow appears to have separated from the bottom wall of the diffuser. The cause of the separation may be due to a manufacture seam where the nozzle array intersects with the diffuser wall. Another potential source of separation is caused by the wave interaction with the boundary layer along the bottom wall. This separation may be a result of the shock wave furthest downstream or the numerous faint waves immediately downstream of the nozzle array, or combinations of both. Without more instrumentation in this region, no conclusions can be made.

4.2 Transition Structure Analysis

The development of an oblique shock on the leading edge of the wedge, which suddenly changes into a normal shock, indicates a rapid rise of pressure in the diffuser that forces the oblique shock upstream toward the nozzles. This pressure rise was associated with a choked condition in the converging transition structure that connected the diffuser to the AFIT facility vacuum line. The minimum area of the transition structure occurs at the downstream exit plane of the transition structure and acts as a second throat for the test apparatus. Procedure #2 was designed to collect data in the

transition structure and determine where and when choking occurred. Figure 4.11 confirms the existence of choked flow in the transition structure.
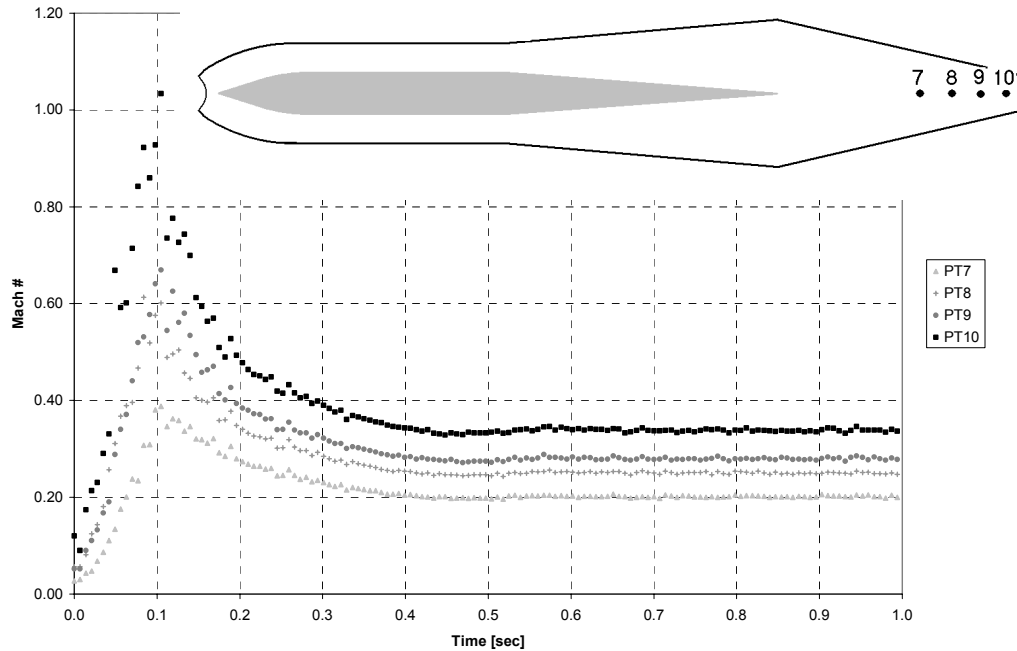
Figure 4.11 Mach Numbers in Transition Structure for Procedure #2

From Figure 4.11, as the area in the transition structure decreased, the Mach number increased, ultimately producing flow that approach sonic conditions. From Figure 4.11, after the first tenth-second from when the wind tunnel was turned on, the Mach number at PT10 reached unity and the transition structure choked. Once the area at PT10 choked, the entire diffuser unstarted as described by Anderson (4). Once the Mach number at PT10 reached unity, the Mach number at each transducer location within the transition structure decreased at a rate similar to that at PT10, as seen in Figure 4.11.

From the data collected during procedure #2, it was noticed that the pressure at PT10 was less than PT11 by as much as 60%. PT10 and PT11 are both plotted in Figure 4.12. The fluctuations in the pressure reading at PT11 are physical in nature and a result

of a sudden deceleration of the fluid from an average of Mach 0.35 to Mach 0.03. The

deceleration is caused by a rapid change in area, and the fluid has likely separated within

this small region of the vacuum line.
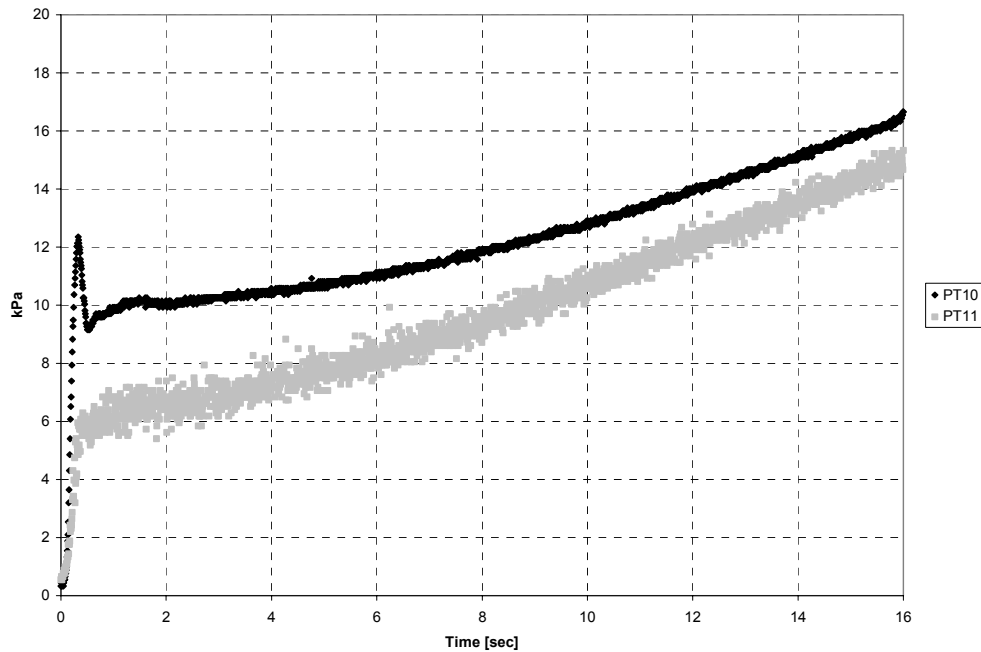
Figure 4.12 Comparison of PT10 and PT11 for Procedure #2

Concerned that hidden expansion waves were present in a region with no instrumentation

prompted analytical calculations to be made and compared to the experimental results.

By taking into account and calculating all expected flow losses from location PT10 to

PT11, accounting for the differences between the pressures to within 10%. The losses

assumed were due only to friction, a single pipe elbow and butterfly valve, and sudden

expansions. As a result, the difference in pressure between PT10 and PT11 is most likely

not due to further expansion of the flow, but rather from head loss caused by friction and

pipe fittings. These calculations are shown in detail in Appendix H and the results

displayed in Figure 4.13. The calculated curve in Figure 4.13 is a good approximation considering the uncertainty of a single pressure reading of +/- 1.8 kPa.
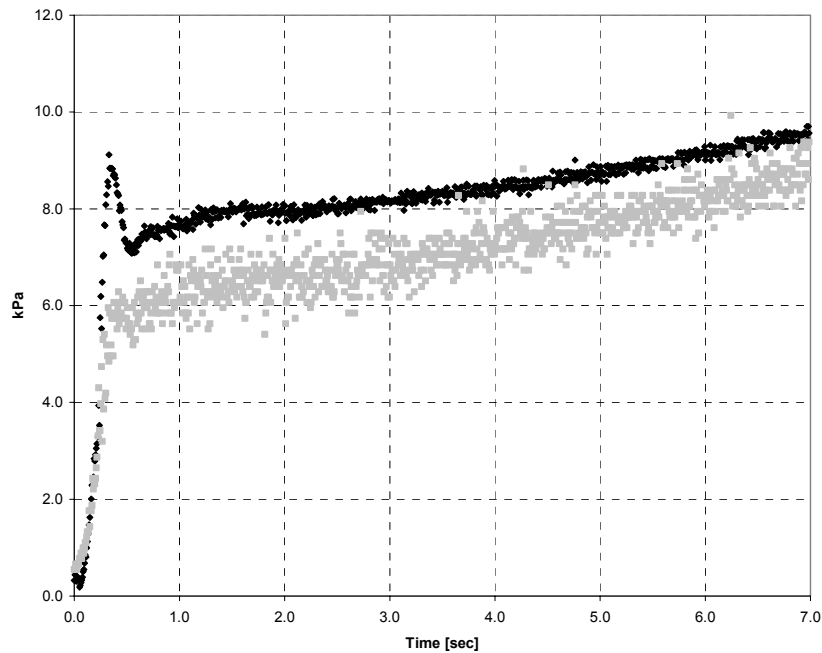
Figure 4.13 Calculated and Experimental Pressures at PT11 for Procedure #2

By resolving the differences in pressures at PT10 and PT11 is reassurance of the Mach numbers displayed in Figure 4.11. If expansion waves were found to exist between PT10 and PT11 well after the transient time interval, then the flow through that region would still be supersonic. Consequently, the diffuser would not unstart and continue to produce supersonic flow.

The ultimate conclusion is that when the wind tunnel was initially turned on, the smallest area of the transition structure was not large enough to swallow the propagating normal shock wave created from the rapid acceleration of the fluid during the transient time interval.

4.3 Solution Attempts

Three attempts were made to remedy the flow from choking in the transition

structure. First, using procedure #1, the reservoir pressure was reduced to the lowest

pressure the wind tunnel pressure regulating system would allow. The goal was to reduce

the Mach numbers throughout the test section by reducing the mass flow, which can be

accomplished by reducing the reservoir pressure. The lowest reservoir pressure

achievable was 59 kPa (8.5 psia) since the regulating system only operated on gauge

pressure and was not able to regulate effectively below atmospheric pressure. Operating

at a reservoir pressure of 59 kPa, the diffuser continued to unstart, yielding the same

schlieren photographs previously displayed in Figure 4.7 and Figure 4.8. The reason can

be found in equation (2).

$$M = \frac{\dot{m}\,RT}{pAa} \tag{2}$$

Reducing the reservoir pressure lowers mass flow rate and static pressure. If they lower

proportionately, no net change in velocity occurs. From Eq. (1), mass flow rate is

directly proportional to the reservoir pressure. Figure 4.14 demonstrates how static

pressure varies with the reservoir pressure. Figure 4.14 graphically displays the effect of

normalizing the pressure at PT2 by the reservoir pressure. If reservoir pressure were

proportional to static pressure, the curves in Figure 4.14 would line up and the ratio of

PT2 to PT1 would be the same regardless of the reservoir pressure. Although the curves

in Figure 4.14 are not identical, the shift in the ratio for various values of PT1 is less than

10%.
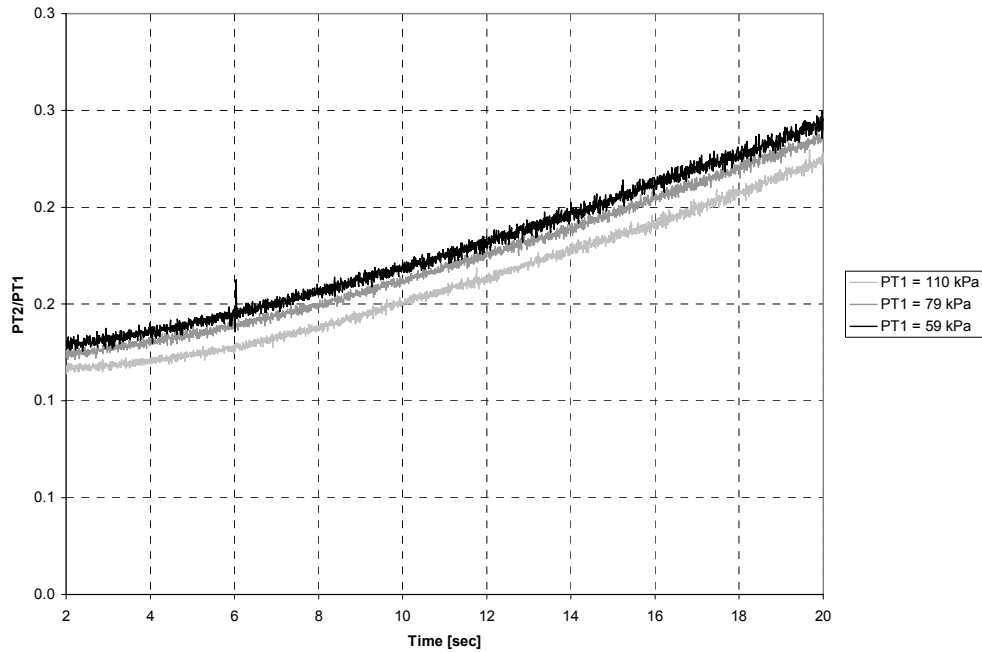
Figure 4.14 Ratio of PT2/PT1 for Procedure #1

Since both mass flow rate and static pressure vary closely with reservoir pressure, Eq. (2) predicts little change in velocity. As a result, the Mach numbers throughout the test section will not vary with ranges of reservoir pressures.

The second attempt to relieve the unstarted diffuser was to reduce the mass flow rate without adjusting reservoir pressure. This was accomplished by reducing the nozzle array throat area by obstructing half the nozzles with metallic tape. Performing procedure #3 yielded the data found in Figure 4.15. The peak recorded Mach number for procedure #3 recorded at PT2 is 56% less than the peak Mach number at the same location for procedure #1. Additionally, the peak Mach number at PT10 is found to be 25% less than the peak Mach number found at PT10 for procedure #2. Both these observations suggest that obstructing half the nozzles in the array has lowered the Mach

4-18

number throughout the test section. However, from the schlieren images (not displayed), the diffuser is still found to unstart
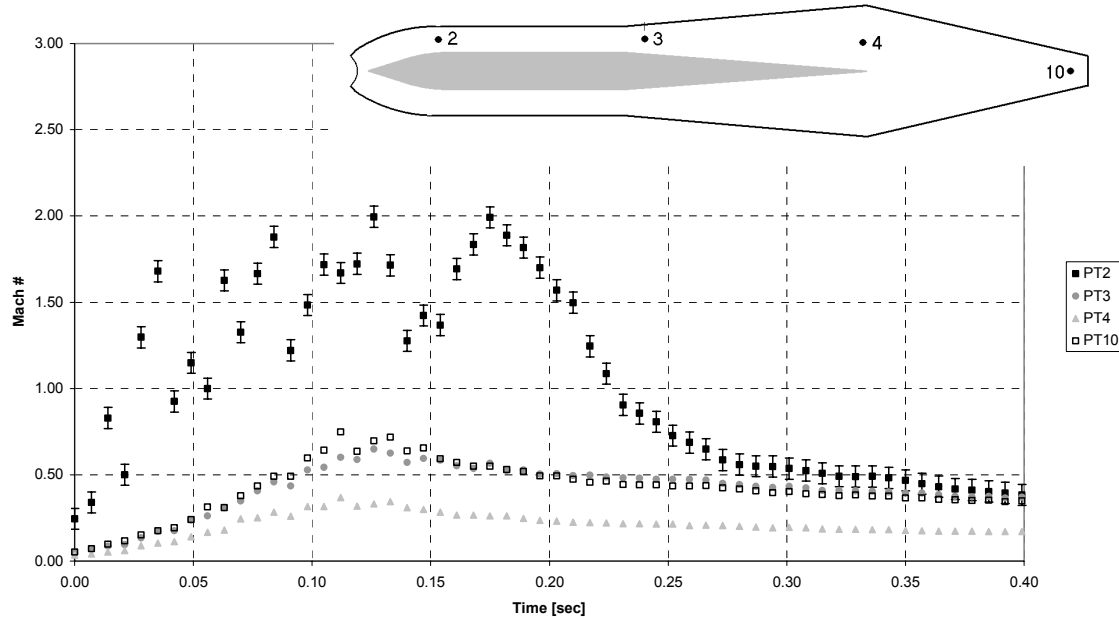
Figure 4.15 Transient Mach Numbers for Procedure #3

The minimum area in the transition structure is still further downstream of PT10. As a result further acceleration and compression of the fluid results. Once the fluid reached the minimum area of the transition structure the Mach number still reached unity and caused a choke point. This is confirmed by calculating the isentropic stream tube relationship found in Eq. (4) for a flow Mach number of 0.75; the peak Mach number in Figure 4.15 at PT10. The calculations revealed the critical area for the flow to reach a Mach number of unity is larger than the minimum area in the transition structure.

Reducing the nozzle array throat area by 50% did reduce the Mach numbers through the test section; however, the diffuser still unstarted. By further decreasing the mass flow rate by reducing the throat area of the nozzle array, the transition structure

would likely not choke. However, this was not explored more in any greater detail. The

disadvantage to obstructing more nozzles is the loss of geometric similarity to the SBL

IFX.

The last attempt to prevent the diffuser from unstarting was successful. By

carrying out procedure #4, no location in the transition structure choked at wind tunnel

startup. This is evident from Figure 4.16.
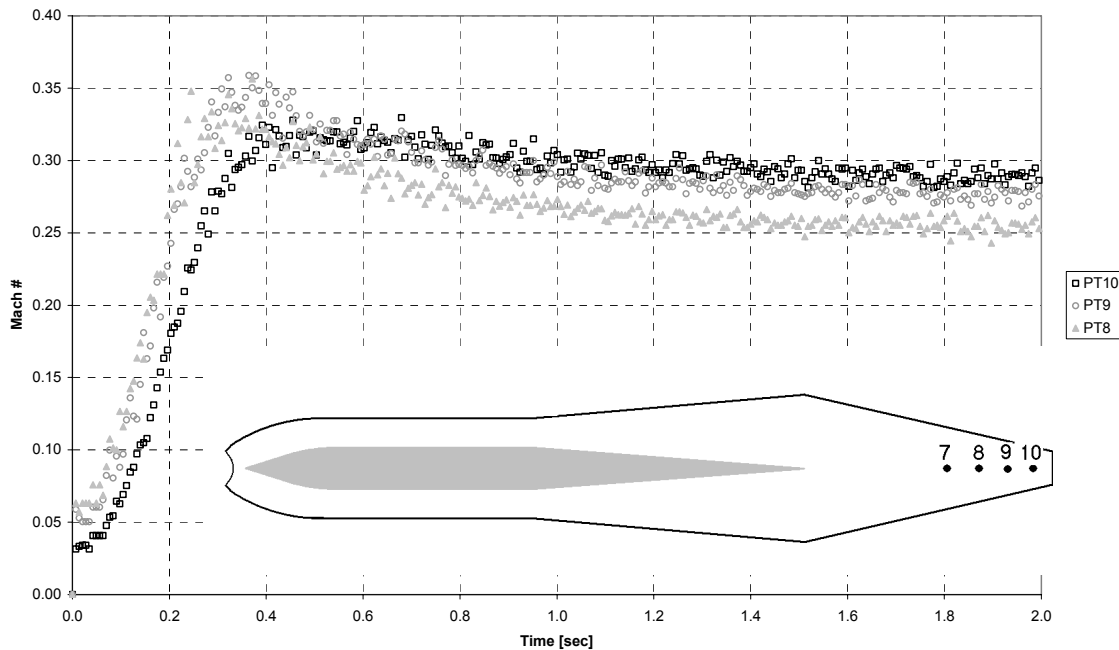
Figure 4.16 Mach Numbers for Initial Two Seconds of Run for Procedure #4

Using wind tunnel circuit #2, the Mach numbers in the transition structure at wind tunnel

startup are 50% less at all pressure transducers than when using wind tunnel circuit #1.

From Figure 4.16, the Mach numbers did not spike as they did in procedures #1-#3. The

peak Mach number at the minimum area of the transition structure is calculated to be

0.53.

Figure 4.16 displays more fluctuation in the calculated Mach numbers than in the previous tests. These fluctuations are physically explainable. Using the ball valve to actuate the wind tunnel, the flow is sucked into the evacuated test section. This is a violent process that causes the ball valve to act as a supersonic throat. Once the flow enters the stilling chamber, it nears stagnation properties but may not completely become still. The calculations for mass flow rate assume the reservoir pressure is a stagnation pressure. This added uncertainty is evident in the data found in Figure 4.16 and propagates in both mass flow and Mach number calculations.
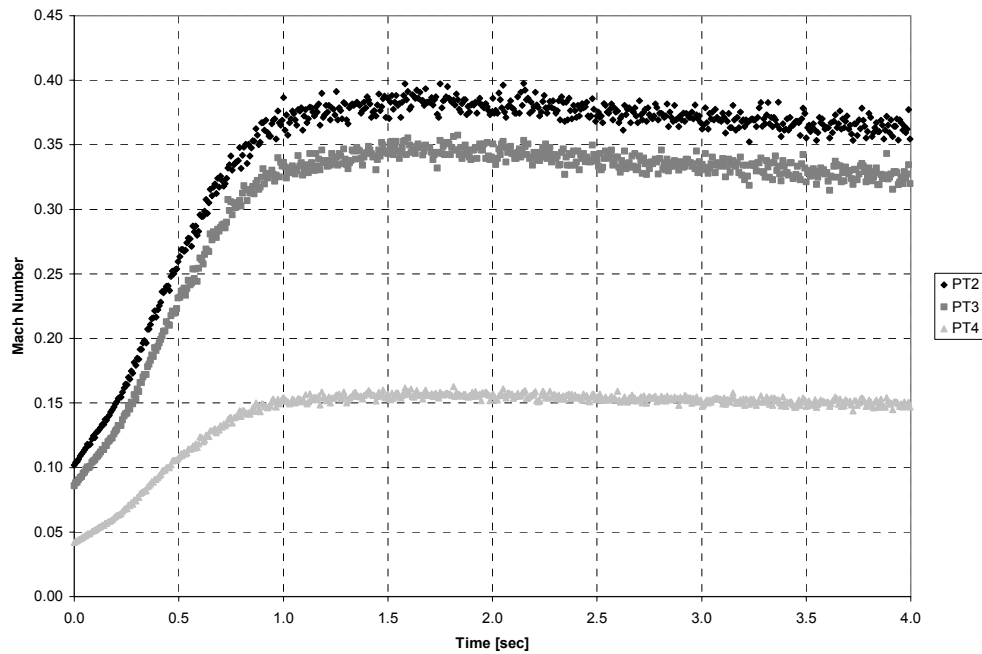
Figure 4.17 Mach Numbers at Beginning of Run for Procedure #5

Knowing the diffuser did not unstart using wind tunnel circuit #2, test procedure #5 was performed and the data displayed in Figure 4.17. At wind tunnel startup, the Mach number at PT2 was accelerated to a maximum of Mach 0.38. After the fluid reached its maximum Mach number at PT2, it decelerated at a rate of Mach 0.0085 per

second. This deceleration was proportional to the increase in back pressure recorded at PT11. The deceleration of the fluid in procedure #5 after reaching a peak Mach number was unlike the rapid deceleration within the transient interval of procedures #1-#3 using wind tunnel circuit #1. The unstarting of the diffuser was a sudden process and is suspected of occurring at the rate the normal shock generated from wind tunnel startup returned upstream through the diffuser. The Mach number gradually decreased and the static pressure gradually increased at PT2 for procedure #5 and was further evidence that the diffuser did not unstart.

For all tests at startup of the wind tunnel, the fluid was accelerated creating a normal shock wave, which propagates down the length of the test section. The total pressure rise across the propagating normal shock wave is at the test section Mach number (4: 173). From Eq. (15), the minimum area of the transition structure was a function of the total pressure rise across the propagating normal shock wave. The stronger the shock wave (the higher the fluid velocity), the larger the total pressure ratio was across the wave. In general, the faster the propagating normal shock wave, the larger the minimum area in the transition structure must be to swallow the shock wave. If the minimum area in the transition cannot swallow the normal shock wave, then the diffuser unstarts.

The maximum calculated Mach number downstream of the leading edge of the centerbody at PT2 for procedure #1 was 3.37 and for procedure #5, 0.38. As was seen from the schlieren image in Figure 4.7, an oblique shock wave is attached at the centerbody during the first 0.1 s of a run for procedure #1, and occurred to within 0-0.2 seconds of the maximum Mach number calculated at PT2 for procedure #1. (The

instrumentation used prevented the exact alignment of the schlieren images and pressure readings in time.) For procedures #1,#3, and #5, if an oblique shock existed at the time of the maximum-recorded Mach number at PT2, then the Mach number upstream of the oblique shock at the centerbody would be larger than the calculated value at PT2. For procedure #1, the Mach number upstream of the centerbody could be greater than Mach 3.37 (as seen in Figure 4.4), assuming the oblique shock wave at t = 0.1 s, Figure 4.7 existed at that moment. Equation (15) dictates that the maximum total pressure ratio possible across the propagating normal shock before the diffuser unstarts is 9.8, and was calculated by dividing the smallest cross-sectional area of the transition structure (assumed to be a second throat) by the total throat area of the nozzle array. This pressure ratio corresponds to a fluid traveling at Mach 4.3. If the Mach number in the test section reached a maximum of Mach 4.3, then the diffuser would theoretically unstart.

Although no pressure readings during any of the five tests yielded calculated Mach numbers of 4.3 or higher at PT2, it is possible that the Mach number upstream of PT2 is 4.3 or higher due to the influence of the shock structure off the centerbody. Additionally, if the propagating normal shock wave were traveling at 1470 m/s (Mach 4.3 at 290K), it would take 1.5 milliseconds to travel through the entire test section. Considering all pressure transducers were sampled every 7 milliseconds, the shock wave could have traversed the test section, not been swallowed by the second throat, and unstarted the diffuser in between pressure recordings.

The difference in maximum Mach numbers at PT2 for procedures #1 and #5 is attributed to the wind tunnel circuit mechanisms used to produce the initial fluid flow. Circuit #1 fills the stilling chamber with a burst of high pressure from the pressure

reducer, which is eventually regulated to the desired pressure. Circuit #2 fills the stilling

pressure with a steady rise in pressure as the ball valve handle is manually turned.

Circuit #1 creates an immediate pressure differential across the nozzles due to the burst of

air into the stilling chamber, resulting in nozzle jets that are grossly underexpanded for an

instant in time. The fluid continues to accelerate downstream of the nozzles to reach

peak Mach numbers of 3.37 at PT2 as seen in procedure #1, Figure 4.4. On the other

hand, the more gradual rise in reservoir pressure associated with circuit #2 does not

produced the same magnitude pressure differential across the nozzles as in circuit #1.

Therefore, jets produced in procedure #5 are not as underexpanded and the fluid does not

need to further expand and accelerate to the degree as the fluid flow in procedure #1.

4.4 Optical Cavity Analysis

The initial oblique shock wave that was attached to the centerbody in the first 0.1

s seen in procedure #1 was not observed in procedure #5. The resulting schlieren image

from procedure #5 is displayed in Figure 4.18. For clarity, Figure 4.19 is a sketch of the

shock structure seen in Figure 4.18.
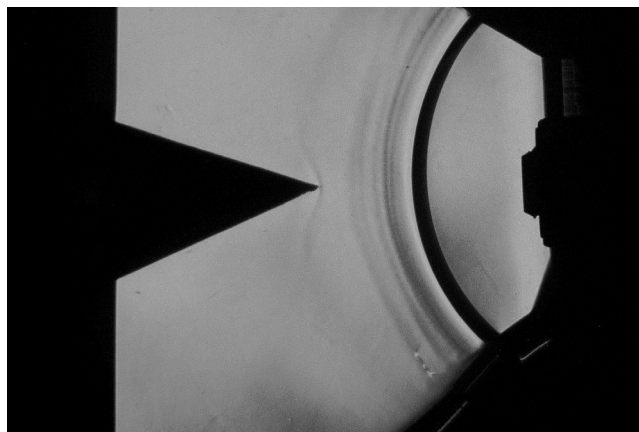
Figure 4.18 Schlieren Photo of Shock Structure for Procedure #5, t = 0-10 Seconds
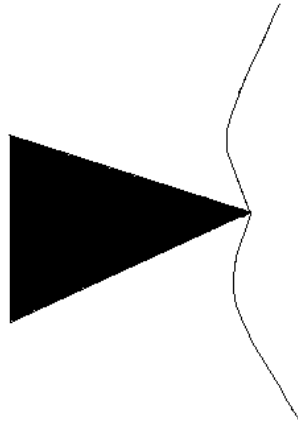
Figure 4.19 Sketch of Shock Structure for Procedure #5, t = 0-10 Seconds

The image in Figure 4.18 was not a transient condition, and lasted 10 seconds before

completely detaching from the centerbody and moving upstream toward the nozzle array.

The angle of the oblique portion of the shock structure was measured, and the Mach

number at the leading edge of the wedge calculated to be Mach 1.9. A Mach number of

1.9 is the minimum Mach number for an attached shock solution to the centerbody.

The shape of the shock structure in Figure 4.18 is interesting and appears to take

on both oblique and normal shock characteristics when considering the angle the

upstream fluid approaches the wave. Evidence that the nozzle array jets are

underexpanded comes from the numerous waves seen upstream of the shock structure in

Figure 4.18. These waves extend downstream a length of 10.25 nozzle widths, which is a

characteristic length of the underexpanded condition found by Bjurstrom (5).

It appears a contradiction exists in the analysis of Figure 4.18. If underexpanded

jets were exuding from the nozzle array, then the flow would further accelerate above the

assumed Mach number at the nozzle exit plane, Mach 1.9. If this were the case, the flow

at the centerbody would be greater than Mach 1.9. However, the Mach number at the

leading edge of the centerbody is determined to be Mach 1.9 from the shock wave angle and suggests that no further acceleration occurs downstream of the nozzle array. The other possibility is that the shock structure is not attached to the centerbody, but is a standing bow shock. This would suggest the flow Mach number at the leading edge of the centerbody was less than Mach 1.9. If this were true, then the jets could not be underexpanded.

From the information collected at PT1 and PT2 for procedure #5, the nature of the steady shock structure seen in Figure 4.18 can be deduced by analytically examining the region. Taking into account the losses through the nozzle array, the total pressure can be calculated at the nozzle exit plane assuming the Mach number is 1.9 as designed. From the image in Figure 4.18, the Mach number at the leading edge of the wedge is known and the static pressure can be calculated. The pressure calculation made downstream of the steady shock structure is for two cases. The first case is that an oblique shock forms off the leading edge of the centerbody, and the second case is that a normal shock forms at the wedge. Since no other shock or expansion waves are expected or observed between the steady shock structure and PT2, the static pressure just downstream of the shock formation and at PT2 should be close in value. Friction losses are negligible since the distance between the leading edge of the centerbody to PT2 is 23 cm. Figure 4.20 displays the points for which pressure was calculated.
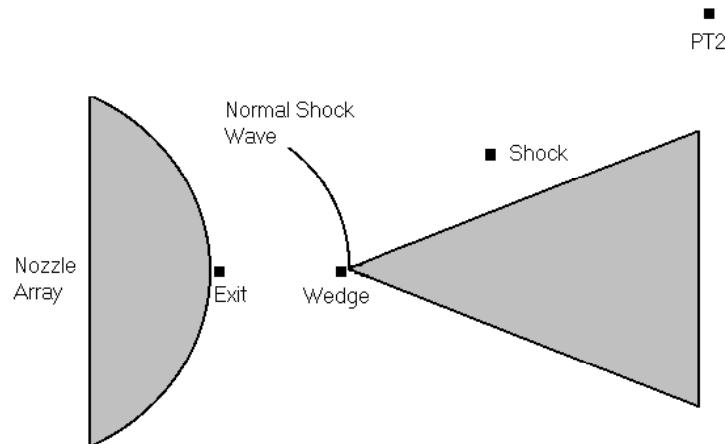
Figure 4.20 Calculation Points for Normal Shock Scenario in Procedure #5

By comparing the calculated static pressure downstream of the shock for the two possible cases to PT2, conclusions can be made about the strength and shape of the shock wave. Figure 4.21 displays the experimental pressure at PT2 and the two calculated static pressures for the two assumed shock structures (at the "shock" calculation node in Figure 4.20).

The calculated static pressure for both cases downstream of the shock structure is larger than the pressure at PT2 by an average of 8600 Pa (1.23 psia). The results in Figure 4.21 were unexpected. Ideally, the static pressure at PT2 should be between the calculated pressures for both cases. This would be consistent with the image in Figure 4.18, since the shock structure displays a combination of an oblique and normal shock orientation to the flow.
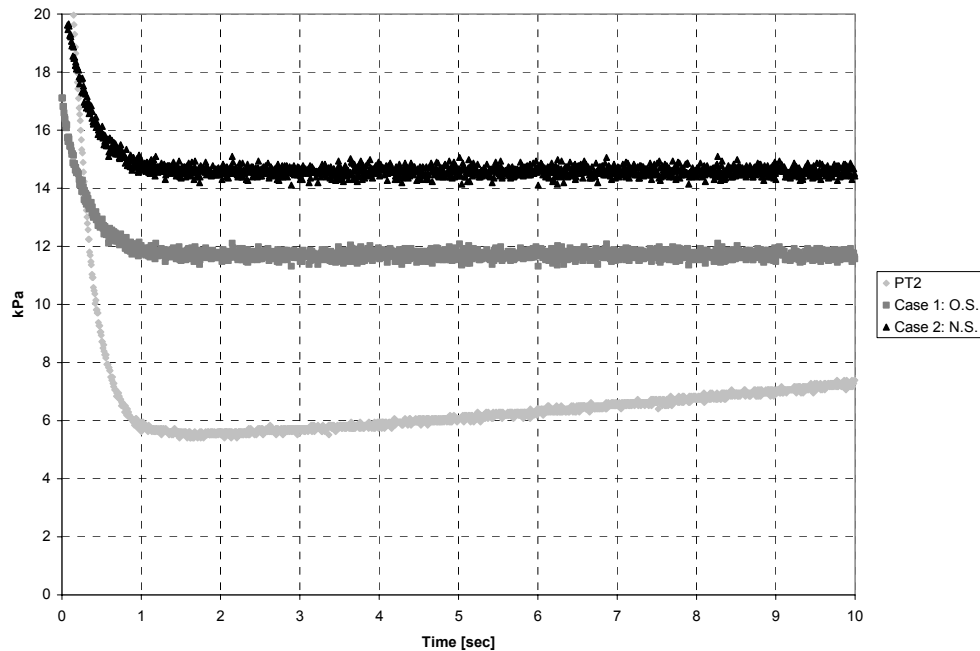
**Figure 4.21 Calculated and Experimental Pressures at PT2 for Procedure #5
(Assume Jets are Underexpanded)**

A couple or reasons may exist for the deviation from expectation. Firstly, the
Mach number at the exit plane of the nozzle array may not be Mach 1.9. If the Mach
number were lower than 1.9 then the calculated pressures in Figure 4.21 would decrease
and move closer to the experimental values of PT2. Secondly, the losses in the distance
from the exit plane of the nozzle array to the leading edge of the wedge may not be
negligible due to turbulent mixing. Additionally, further losses in total pressure would
exist if the multiple jets were overexpanded and not underexpanded as a result of the
oblique shock waves forming at the nozzle exit plane.

Assuming the multiple jets to be overexpanded rather than underexpanded as first
assumed, and a 20% loss in total pressure from the nozzle array to the wedge, the
calculated pressures better align with the readings at PT2.
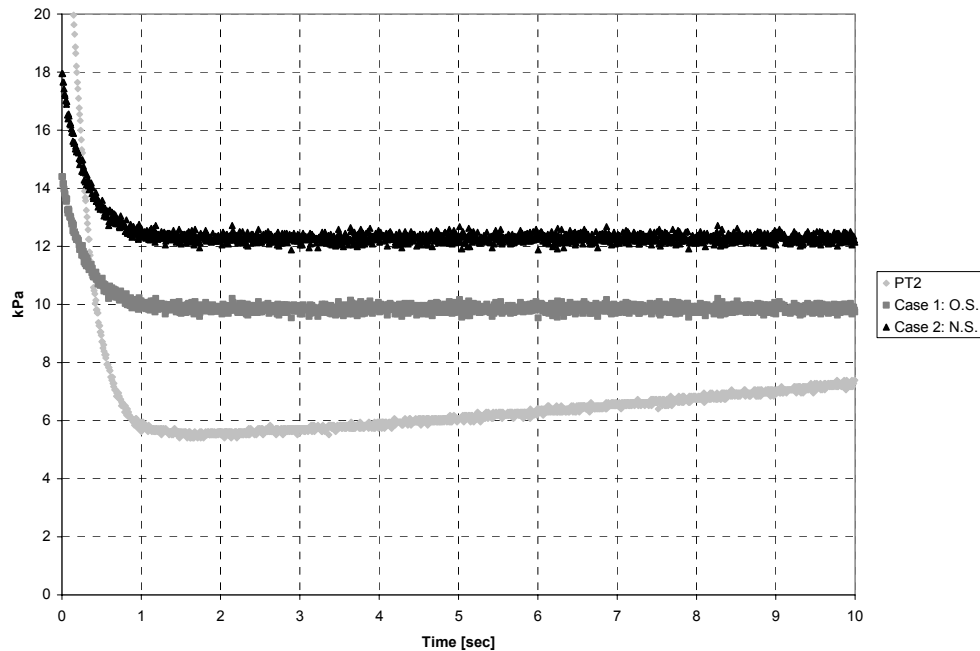
**Figure 4.22 Calculated and Experimental Pressure at PT2 for Procedure #5
(Assume Jets are Overexpanded)**

Figure 4.22 is a comparison of calculated and experimental pressures at PT2 having

assumed that the jets are overexpanded. Figure 4.22 indicates that by assuming more

losses across the distance from the nozzle array to the leading edge of the wedge, the

calculated and experimental data are closer than in the previous figure. However, the

calculated and experimental curves in Figure 4.22 are off by a factor of two and reveal

that the flow through the optical cavity for procedure #5 is still not understood.

The calculations made to generate Figure 4.21and Figure 4.22 are located in

Appendix I. These calculations were attempts to better understand the shock structure

and were largely based on assumptions. The largest source of error in the approximations

made may be that the shock structure observed in procedure #5 could be analyzed with

two-dimensional shock jump relations. The model created was three-dimensional, and

due to the turbulent mixing of the jets, the effects of the third dimension were not

4-29

negligible. All schlieren pictures were views across a non-uniform flow field that was 6.6-cm in depth. Consequently, what is seen in all schlieren images is an instantaneous spatial average. The shock structure seen in Figure 4.18 may not be a typical oblique or normal shock wave that can be easily analyzable. To better understand this three-dimensional flow requires more instrumentation, especially in the optical cavity of the diffuser.

4.5 Final Thoughts

Readdressing the topic of similarity of the subscale model to the full-size SBL IFX, the transient time interval of procedure #1 proved to be the most similar in terms of shock structure and Mach number to the numerical results found by TRW than any other time or procedure. However, the Reynolds number at the leading edge of the centerbody during this transient time interval was previously calculated to potentially be greater than the TRW results by an order of magnitude during the transient condition. The Reynolds number calculated at the leading edge of the centerbody for the subscale model is proportionally dependent on the reservoir pressure. To better simulate the TRW numerical Reynolds number, the reservoir pressure must be lowered. For procedure #1, the lowest reservoir pressure achievable was 59 kPa (8.5 psia) due to the inability of the pressure regulating system. Therefore, the pressure regulating system was by-passed using wind tunnel circuit #2. In further reducing the reservoir pressure by modifying the wind tunnel circuit, the highest Mach number found in the optical cavity during the transient time interval of procedure #1 were not duplicated. It was determined using procedure #5 that the minimum reservoir pressure required to produce supersonic flow from the nozzle array was 17 kPa (2.5 psia).

If a pressure regulating system allowed the same sudden acceleration of the fluid found in procedure #1 but the same minimum reservoir pressure to start the nozzle array as in procedure #5, could the Reynolds number in the subscale model better match TRW's calculations? If this were the case, the jets would not be as underexpanded and the flow would not accelerate to the same Mach number found in procedure #1. Although the velocity at the leading edge of the centerbody would be less, the static pressure and temperature would be larger than when Reynolds number was calculated for procedure #1. The effect this would have on the Reynolds number is unknown and hypothetical.

5. Conclusions and Recommendations

5.1 The First Objective

The first objective of this research was to build a modular test section capable of investigating the flow conditions in a simulated laser nozzle assembly using cold-flow, and that the test section must be modular. This objective was met with moderate success. To achieve the highest quality laser possible, the flow within the lasing cavity would look more like the transient oblique shock wave found in procedure #1 for longer duration. At this condition, the fluid was found to be at the maximum Mach number achievable throughout the lasing cavity. Furthermore, the only shock structure found to exist at this instant was the oblique shock wave attached to the leading edge of the centerbody, which would be less obtrusive to laser formation than any other shock structure.

The choke point in the transition structure was deemed the cause for the brevity of the transient oblique shock wave within the optical cavity. The transition structure is not part of the SBL IFX, but was a necessary means to mate the test section to the AFIT wind tunnel. Dr. John Anderson (4) states "...the design of a diffuser for a given application must be based on empirical data and inspiration. Rarely is the first version of the new diffuser ever completely successful." This statement is certainly true of the transition structure created for this research. For future research to occur using wind tunnel circuit #1, the transition structure must be redesigned to allow for wind tunnel startup. By preventing the diffuser from unstarting, supersonic flow within the optical cavity may last longer, and provide a better opportunity to collect information.

By modifying the wind tunnel to create wind tunnel circuit #2, mixed success resulted. The flow remained supersonic through the critical space between the nozzle array and the centerbody, but became subsonic closer to the top and bottom walls of the diffuser. It was determined that by gradually increasing the reservoir pressure using wind tunnel circuit #2, the jets where not as underexpanded as when using wind tunnel circuit #1. Consequently, the maximum Mach number within the optical cavity using circuit #1 was significantly less than when using circuit #1. The conclusion is that to duplicate the ideal flow structure, the faster the reservoir pressure is established the better.

5.2 The Second Objective

The second objective was to determine the operating characteristics of the nozzle/diffuser system. The fundamental aspects were determined, and more instrumentation is required to fully understand all aspects of the fluid flow throughout the diffuser. The largest contribution to the SBL IFX body of knowledge through this research is the mapping of velocities in regions of the diffuser. At the downstream end of the diffuser, the fluid flow was always subsonic and possibly approach incompressible flow. This was true even before the diffuser unstarted. The flow in the center of the diffuser was subsonic at all times.

Schlieren photography revealed that faint waves are present 10-15 nozzle widths downstream of the nozzle array when the flow was expected to be underexpanded. These waves are thought to be intersecting expansion and compression waves inside each jet plume, but were not observed during the transient region due to the resolution of the video recorder. If these faint waves can conclusively be determined to be part of the

shock diamond pattern in an underexpanded jet, they would exist during the transient time frame also.

5.3 Recommendations

The following is a list of possible improvements in better achieving the two objectives initially embarked upon:

1) Redesign the transition structure to prevent the diffuser from unstarting at wind tunnel startup using wind tunnel circuit #1

2) Place thermocouples at all pressure transducer locations

3) Develop a means to measure the Mach number at the exit of the nozzle array

4) Verify that the faint waves 10-15 nozzle widths downstream are part of the shock diamond pattern of a typical underexpanded jet

5) Place a matrix of pressure transducers along top wall of diffuser in the region where diffuser is turning the fluid from the radial direction to the horizontal direction

6) Measure the pressure at base regions of the nozzle array

7) Remanufacture nozzle array to produce faster exit plane Mach number to allow oblique shock wave at centerbody to remain attached longer and maintain supersonic flow

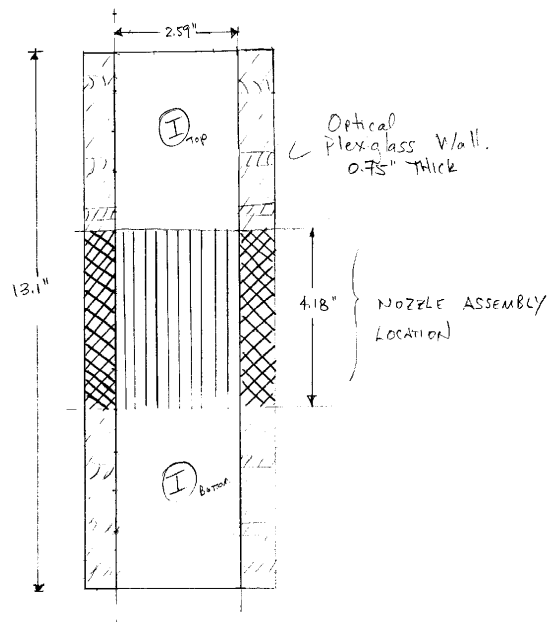8) Replace pressure reducer with a device that can regulate the reservoir pressure to a lower range

Appendix A: Calculation of Losses Through Non-isentropic Nozzle

To gain knowledge of what types of losses will occur with a non-contoured nozzle wall, a single nozzle was manufactured. The nozzle built was simply a linear nozzle and unlike the nozzles created for the model. It was created with no contour in the nozzle wall. The expansion ratio was 1.44 and would have yielded a Mach number of 1.8.

The nozzle was bolted to the wind tunnel stilling chamber with the exit open to the atmosphere. A stagnation pressure of 35 psi in the stilling chamber resulted in a pressure ratio across the nozzle of approximately 2.5 when venting to atmosphere.

A schlieren picture was projected onto a white piece of cardboard. A small metal wedge was placed in the flow (1 mm away from the nozzle exit plane) with a half angle of 7.5 degrees. Once the flow started, an oblique shock wave was created off the leading edge of the wedge at an unknown angle. The picture was sketched onto the cardboard while the wind tunnel was running. The shock wave angle was measured with a protractor to be 53-degrees. Knowing the relationship between the wedge half angle and the angle of the shock wave, the Mach number at the wedge was estimated to be Mach 1.5. Due to losses inside the sample nozzle, a 15% deviation from the isentropic expansion Mach number can be deduced.

Appendix B: Diagram of Diffuser

I   II   III

Top

21.2"

25.6"

~6°

2.69"

Bottom

plexiglass wall
0.75" thick

Aluminum Sheet
Wall 0.190" thick

I   2 blocks = 1 inch

8.81"

1/8" O-RING GROOVE

0.75"

1/8" O-RING GROOVE

4.4"

1.00"

ORIGIN

FOR PURPOSE OF
X-Y COORDINATES TO
CONSTRUCT CURVATURE

1.00"

2.59"

I top

Optical
Plexiglass Wall.
0.75" THICK

13.1"

4.18"   NOZZLE ASSEMBLY
LOCATION

I bottom
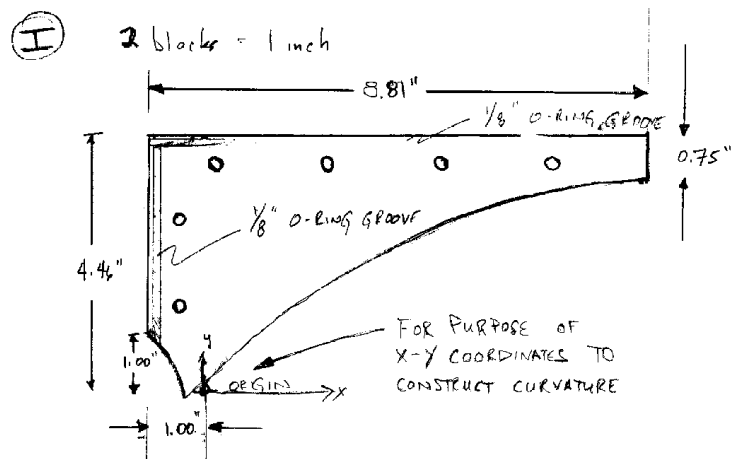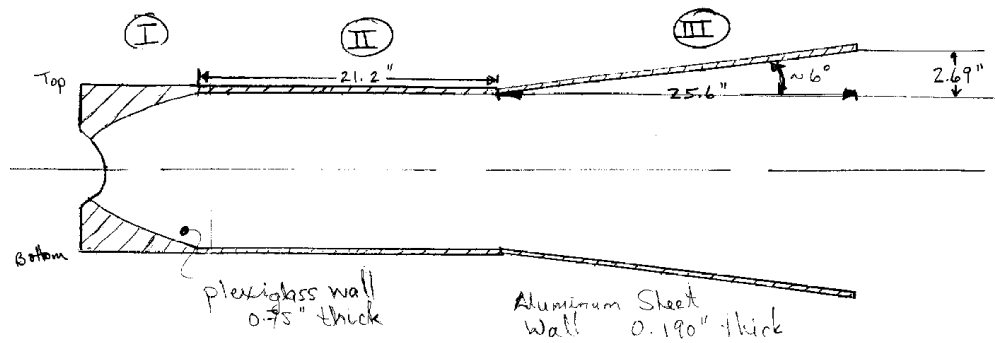
Appendix C: Uncertainty Analysis

An uncertainty analysis was performed for the instrumentation used to determine the

accuracy for a single pressure reading. This analysis was provided by Wheeler and Ganji

(15: 178-182). The following is a list of calibration errors broken down by

instrumentation component. The Full Scale (FS) of the transducers was 50 psia.

Pressure Transducer:

Nonlinearity and hysteresis = +/- 0.1% FS

Repeatability = +/- 0.1% FS

Thermal sensitivity shift = +/- 0.015%/⁰F

Pressure Signal Conditioner:

Gain error = +/-0.5% FS

The calibration errors were categorized into bias and precision uncertainties. The only

bias error in the system due to the pressure transducer was the nonlinearity and hysteresis

uncertainties and found to be:

$$B_1 = \frac{0.1}{100}(50\,psia) = \pm 0.05\,psia$$

The precision error due to the pressure transducer was from the repeatability and thermal

sensitivity shift. To ensure the uncertainty was with a 95% confidence level, the degrees

of freedom were assumed to be 30. When referencing a tabulated form of the Student's t-

distribution, t = 2. The precision indices could be estimated:

$$S_{repeatibility} = S_1 = \frac{(0.1\%)(FS)}{(100)t} = 0.025\,psia$$

$$S_{thermal} = S_2 = \frac{(0.015)(T_{shift})(FS)}{(100)t} = 0.0075\,psia \text{ where } T_{shift} = \pm 2^0 F.$$

The single uncertainty of the signal conditioner was a bias uncertainty. The error was

calculated:

$$B_{gain} = B_2 = \frac{(\pm 0.5\%)(FS)}{100} = 0.25\,psia$$

By combining all the bias and precision errors of the system, a total bias and precision

error was calculated:

$$B_T = \left(B_1{}^2 + B_2{}^2\right)^{\frac{1}{2}} = 0.255\,psia$$

$$S_T = \left(S_1{}^2 + S_2{}^2\right)^{\frac{1}{2}} = 0.0261\,psia$$

Finally, the estimated uncertainty for a single pressure reading could be found:

$$\boxed{w_T = \left(B_T{}^2 + tS_T{}^2\right)^{\frac{1}{2}} = 0.261\,psia = 1793\,Pa}$$

Therefore, the uncertainty in a pressure reading was $\pm 0.3\,psia$ (2000 Pa) with 95%

confidence level considering significant figures.

Calculated Results:

The maximum error in the calculations performed for mass flow and Mach number was

investigated considering the uncertainty in pressure. Recall the mass flow equation:

$$\dot{m} = \frac{p_t}{\sqrt{RT_t}} A\sqrt{\gamma}\left(1 + \frac{\gamma-1}{2}M^2\right)^{\frac{\gamma+1}{2-2\gamma}}$$

Taking the partial derivative with respect to the total pressure, and applying the equation

to the nozzle throat:

$$\frac{\partial \dot{m}}{\partial p_t} = \frac{A\sqrt{\gamma}\left(1 + \frac{\gamma-1}{2}M^2\right)^{\frac{\gamma+1}{2-2\gamma}}}{\sqrt{RT}} = 2.61E - 6$$

$$w_{p_t} = 1793 Pa$$

Therefore, the max error in the mass flow calculations was determined to be:

$$\boxed{\begin{aligned} w_{\dot{m}} &= \frac{\partial \dot{m}}{\partial p_t} w_{p_t} = (2.61E-6)(1793) \\ w_{\dot{m}} &= 4.7E - 3 kg/s \end{aligned}}$$

The Mach number equation is:

$$M = \frac{\dot{m}RT}{pA\sqrt{\gamma RT}}$$

The sources of error in this equation are due to the mass flow calculation, uncertainty in pressure reading, and temperature fluctuations. The temperature within the test section was assumed to range +/- 10 K during the run.

$$w_T = 10 K$$
$$w_p = 1763 Pa$$
$$w_{\dot{m}} = 4.68E - 3 kg/sec$$
$$\frac{\partial M}{\partial \dot{m}} = 2.97$$
$$\frac{\partial M}{\partial p} = -3.33E - 5$$
$$\frac{\partial M}{\partial T} = 0.0015$$

To find the maximum error in Mach number:
$$\boxed{\begin{aligned} w_M &= \frac{\partial M}{\partial \dot{m}} w_{\dot{m}} + \frac{\partial M}{\partial p} w_p + \frac{\partial M}{\partial T} w_T \\ w_M &= 0.1 \end{aligned}}$$

Appendix D: Calculation of Vacuum Line Head Loss

These analytical calculations were performed to determine the initial pressure rise
through the 73-foot long vacuum line when the wind tunnel was started. The pressure at
PT11 was used to determine velocity and density. The cross-sectional area at the PT11
was 270 in^2 (0.174 m^2).

Calculate mass flow applied at the nozzle throat:

$$\dot{m} = \frac{p_t}{\sqrt{RT_t}} A\sqrt{\gamma}\left(1 + \frac{\gamma-1}{2}M^2\right)^{\frac{\gamma+1}{2-2\gamma}}$$

where,

$\gamma = 1.4$

A$_t$ = 0.0011 m^2

p$_t$ = 16$psia$ = 110.32 kPa

T$_t$ = 290 K

R = 287 KJ/kgK

M = 1

Therefore, $\dot{m} = 0.28$ kg/s

By using the pressure at the PT11 immediately after the initial rise in pressure as is seen
in Figure 4.2:

p$_{11}$ = 1.3 psia = 8963.5 Pa

Calculate average velocity in vacuum line:

$$V_{11} = \frac{\dot{m}RT}{p_{11}A_{11}}$$

$$V_{11} = \frac{(0.28kg/s)(287KJ/kgK)(290K)}{(8963.5Pa)(0.174m^2)}$$

$$V_{11} = 14.94m/s$$

Assuming the flow was incompressible, determine the velocity in the constant area vacuum line immediately downstream of the area where PT11 was located.

$$V_{line} = \frac{V_w A_w}{A_{line}}$$

where $A_{line} = 44.2in^2 = 0.028m^2$

$$V_{line} = \frac{(14.07m/s)(0.174m^2)}{(0.028m^2)}$$

$$V_{line} = 87.44m/s$$

Need to determine Reynolds number and classify flow as turbulent or laminar.

$$\mathrm{Re}_D = \frac{\rho V D}{\mu}$$

Using Sutherland's Law, find μ.

$$\mu = \frac{bT^{\frac{3}{2}}}{S+T}$$

where,

b=1.458E-6 and

S=110.4 K

$\mu = 1.82$E-5 Ns/m^2

Calculate density using ideal gas law and the static pressure used early for p_{11}.

$$\rho = \frac{p}{RT} = \frac{8963.5Pa}{(287kJ/kgK)(290K)} = 0.108kg/m^3$$

D-2

Consequently,

$$Re_D = \frac{(0.108 kg/m^3)(87.44 m/s)(0.1905 m)}{1.82E - 5 Ns/m^2}$$

$$Re_D = 97,242$$

For internal pipe flow, the transition Reynolds number is roughly 2,000. Therefore, the assumption was that the fluid was turbulent within the vacuum line. The first losses to be calculated were those caused by friction and calculated by equation (12):

$$h_l = f \frac{L}{D} \frac{\overline{V}^2}{2}$$

The friction factor was estimated to be 0.03. Therefore,

$$h_l = (0.03) \frac{(22.25 m)}{(0.1905 m)} \frac{(87.44 m/s)^2}{2}$$

$$h_l = 14000 m^2/s^2$$

Furthermore, the minor losses associated with pipe bends were determined using equation (13):

$$h_{lm} = f \frac{L_e}{D} \frac{\overline{V}^2}{2}$$

where the L_e/D was called the equivalent length and found in mechanical engineering handbooks. For the six 90 deg elbows with a radius of 1 foot, the equivalent length used equals 25. The two 45 deg elbows, the equivalent length used was 12 (6:366).

$$h_{lm} = (0.02) \frac{(87.44)^2}{2} [6(25) + 2(12)]]$$

$$h_{lm} = 13304 m^2/s^2$$

Furthermore, sudden contractions and expansions was factored into the overall losses.

A sudden contraction occurs from the void where PT11 was located to the vacuum line.

The contraction ratio $\dfrac{A_{line}}{A_{11}} = 0.164$. An expansion exists at the end of the vacuum line

when the fluid was dumped into the 6000-gallon cylindrical vacuum tank. The expansion

ratio was $\dfrac{A_{line}}{A_{\tan k}} = 0.016$. Using Equation (14) and looking up the loss coefficients based

on the contraction/expansion ratios:

$$h_{l,e/c} = \frac{\overline{V}^2}{2}(K_e + K_c)$$

$$h_{l,e/c} = \frac{(87.44)^2}{2}(0.9 + 0.45)$$

$$h_{l,e/c} = 5160 m^2 / s^2$$

By adding all three types of losses together,

$$h_{l,T} = 32000 m^2 / s^2$$

Using equation (11), this head loss was transformed into a change in pressure:

$$\Delta p = h_{l,T}\rho = (32000 m^2 / s^2)(0.108 kg / m^3)$$

$$\Delta p = 3450 Pa = 0.5 psi$$

Appendix E: Back Pressure Analysis

Derivation:

$$m = \Lambda\rho$$

$$\rho = \frac{p}{RT}$$

$$p = \frac{mRT}{\Lambda}$$

Put in differential form

$$\frac{dp}{dt} = \frac{RT}{\Lambda}\frac{dm}{dt}$$

$$\frac{dp}{dt} = \frac{RT\,\dot{m}}{\Lambda}$$

Vacuum tank had a volume of 6000 gallons.

$$\Lambda = 6000 \text{ gallons} = 22.71m^3$$
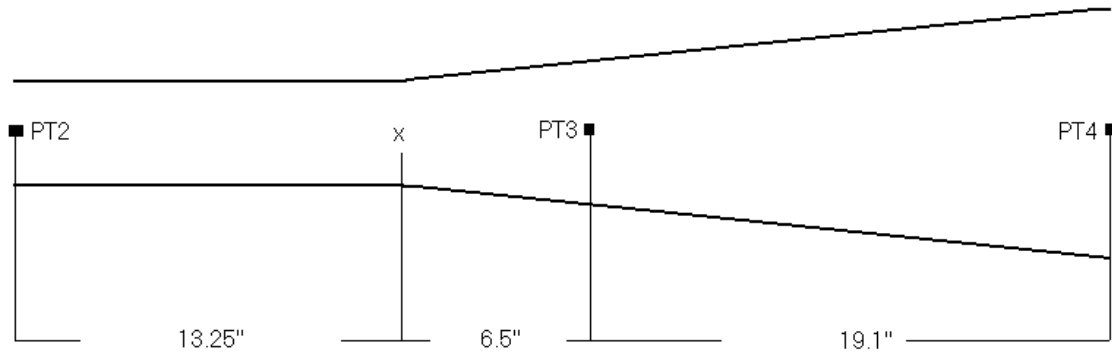
Therefore, using the mass flow found in Appendix D and assuming the temperature was a constant:

$$\frac{dp}{dt} = \frac{(287KJ/kgK)(290K)(0.28kg/s)}{22.71m^3}$$

$$\frac{dp}{dt} = 1026.17Pa/s$$

$$\frac{dp}{dt} = 0.15psi/s$$

Appendix F: Analytical Pressure Calculations Within Diffuser

The steady-state recorded pressures from the four transducers located within the diffuser could easily be compared to theory. The following analysis was performed using average Mach numbers at each transducer location. The Mach numbers were averaged over a 5 second interval within the steady-state time frame. The distance from PT2 to PT3 was 19.75 in. From PT2 to x, a one-dimensional Fanno analysis was performed to determine the effect on Mach number. Since the cross-sectional area is rectangular, a hydraulic diameter was used:

$$D_h = \frac{4A}{P} = 3.025 in$$

where P is the perimeter of the cross-sectional geometry. The average Mach number at the PT2 is 0.4. At this Mach number, the critical length was found to be:

$$\frac{fL^*}{D} = 1.92$$

Calculating the same ratio with the physical characteristics of the rectangular channel with an assumed $f = 0.02$ and $L = 13.25 in$:

$$\frac{fL}{D_h} = 0.0876$$

By subtracting the two values:

$$\left(\frac{fL^*}{D}\right)_x = \left(\frac{fL^*}{D}\right)_{PT2} - \frac{fL}{D_h} = 1.83$$

this ratio corresponds to a Mach number at the end of the constant area section of the diffuser equal to 0.43. As a result, little effect due to friction was determined. Assuming the fluid was incompressible as the area expands, the Mach number at the PT3 became:

$$M_{PT3} = \frac{M_x A_x}{A_{PT3}} = \frac{(0.43)(9.4in^2)}{11.3in^2} = 0.36$$

Using Eq (2) and the experimental static pressure, an average Mach number at PT3 was determined to be 0.327. From the PT3 to PT4, the flow was expanding and assumed to be incompressible. Therefore, the Mach number at the PT4 was calculated:

$$M_{PT4} = \frac{M_{PT3} A_{PT3}}{A_{PT4}} = \frac{(0.358)(11.3in^2)}{23.3in^2} = 0.17$$

The average experimental Mach number at PT4 (calculated with the experimental static pressure and Eq (2)) was 0.18, and was within 6% of the theoretical Mach number at this location.

Appendix G: Test #1 Transient Schlieren Photo Sequence

G-2
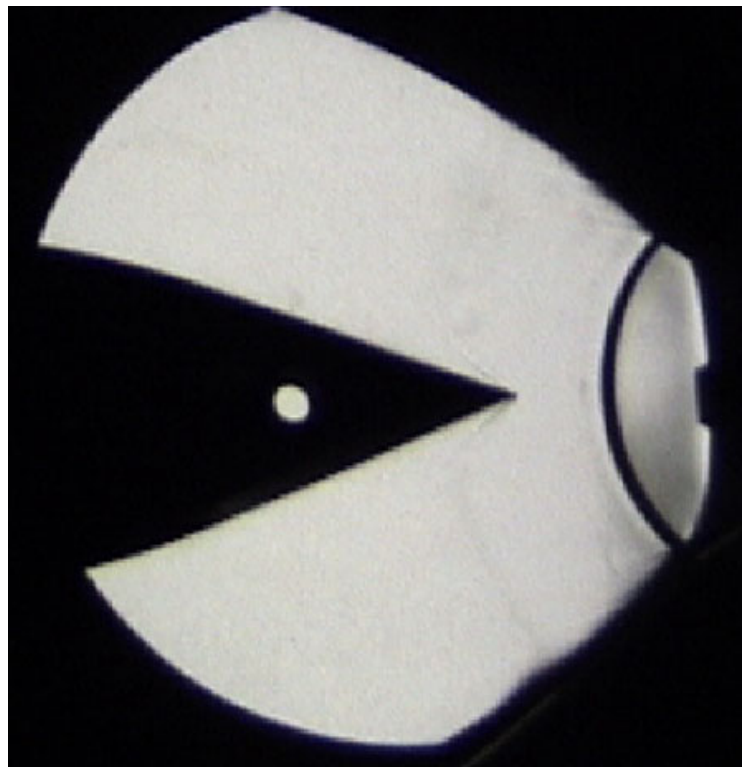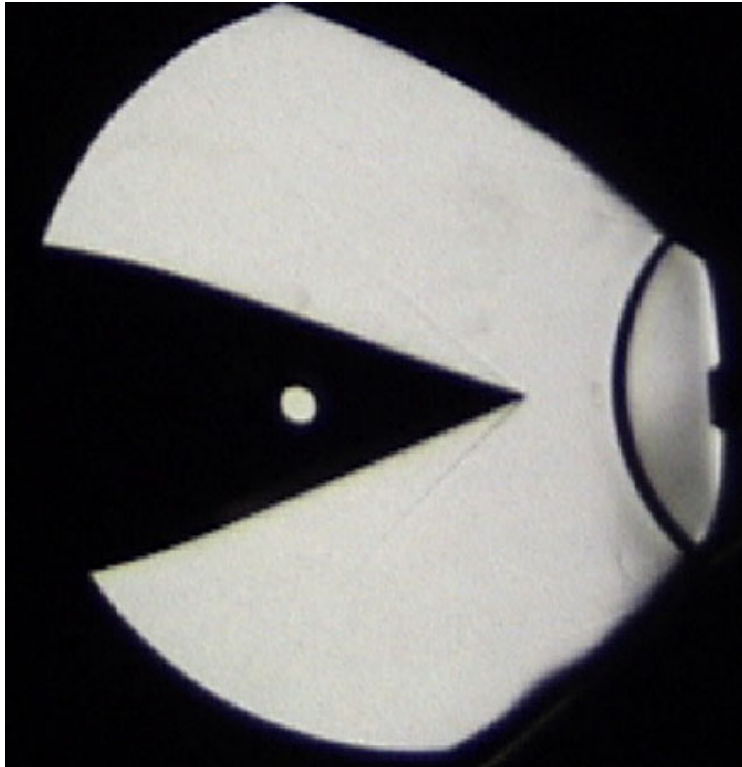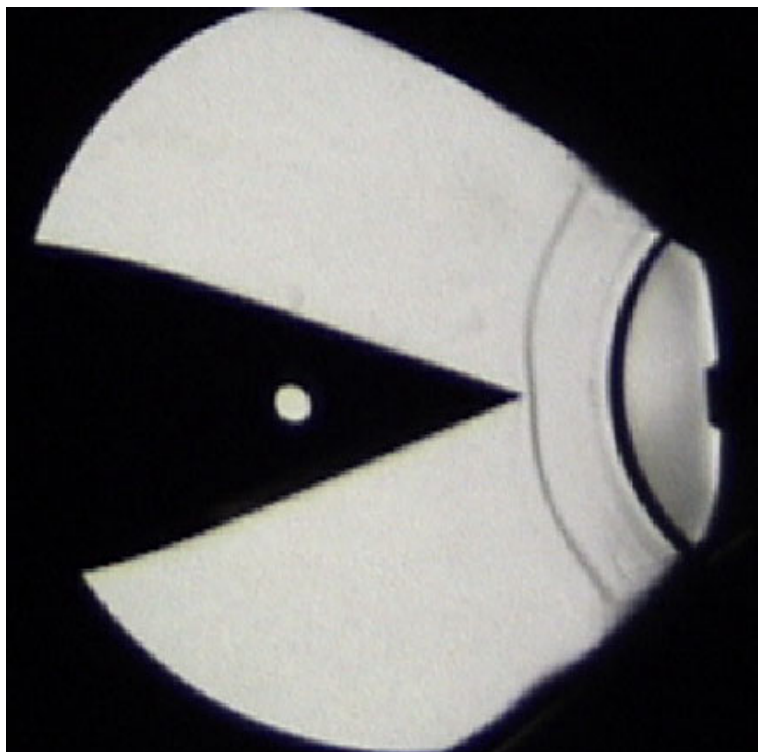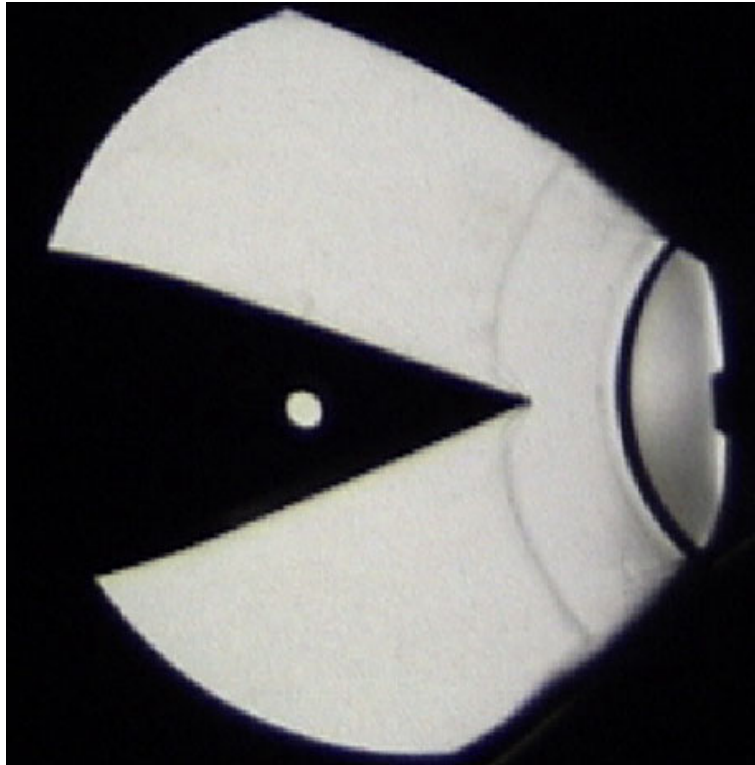
Appendix H: Pressure Analysis Between PT10 and PT11
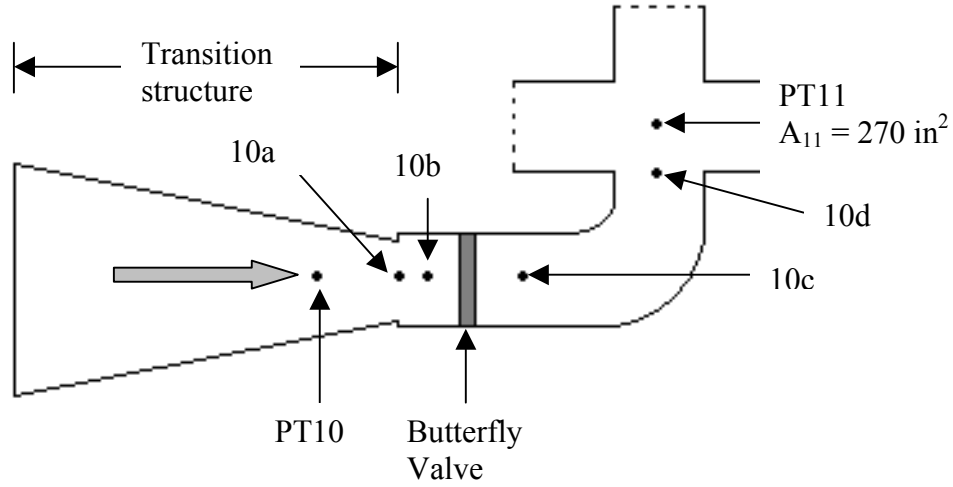
The only ports used for experimental pressure measurements were PT10 and PT11.

References 10a-10d were locations where values were estimated based on analytical

calculations. If information gathered at PT10 was used as a starting point and losses

across each station are calculated, the result was an analytical expression at PT11 that

matches the experimental data. First, it was estimated that the flow from 10a to PT11

was isentropic. Therefore, equations for the Mach number and stream tube ratio at PT10

are:

$$M_{10} = \frac{\dot{m}\, RT}{p_{10} A_{10} \sqrt{\gamma RT}}$$

and,

$$\frac{A_{10}}{A^*} = \frac{\sqrt{\gamma}\left(\dfrac{\gamma+1}{2}\right)^{\frac{\gamma+1}{2-2\gamma}}}{M_{10}\sqrt{\gamma}\left(1+\dfrac{\gamma-1}{2}M_{10}^{\,2}\right)^{\frac{\gamma+1}{2-2\gamma}}}$$

From PT10, the stream-tube ratio can be found at 10a:

$$\frac{A_{10a}}{A^*} = \frac{A_{10a}}{A_{10}}\frac{A_{10}}{A^*}$$

Through iteration, solved for the Mach number at 10a via the stream tube equation. Once the Mach number was known, the pressure could be solved for at 10a. Assuming the Mach number at 10a was subsonic (as was found to be true during test procedure #4), the fluid will suddenly decelerate, once it travels through the exit plane of the transition structure and into the much larger area of the vacuum line. Due to the lack of information in this region of the vacuum line, the fluid was assumed to be incompressible. This may prove to be a poor assumption; especially considering the range of Mach numbers was from 0.5 to 0.1. As a result, a certain amount of inaccuracy was admittedly accepted for the purposes of this analysis. The Mach number at 10b was found using conservation of mass:

$$M_{10b} = \frac{M_{10a}A_{10a}}{A_{10b}}$$

The pressure at 10b could be solved for using the Mach number, and given the subscript "isentropic" due to a lack of consideration of any losses induced on the fluid as it travels through the incremented passage.

$$p_{10b,isentropic} = \frac{\dot{m}\,RT}{M_{10b}A_{10b}\sqrt{\gamma RT}}$$

The loss in pressure due to a sudden expansion could not be overlooked. From port 10a to 10b the area ratio was 0.38, which according to Fox & McDonald results in a loss coefficient of 0.4.

Therefore,

$$h_{l,e} = K_e \frac{\overline{V}^2}{2}$$

$$\Delta p_{10a-10b} = \rho h_{l,e}$$

where the density is assumed to be a constant and found as an average throughout a single run. Now that the change in pressure has been determined, the pressure at 10b was determined to be:

$$p_{10b} = p_{10b,isentropic} - \Delta p_{10b-10a}$$

10b and 10c have the vacuum butterfly valve that separate them. A change in pressure across the valve can be determined by means of a loss coefficient that can be found in the literature. For this calculation the value for the loss coefficient was found on a commercial internet page. For a 7.5 inch diameter butterfly valve, K is equal to 0.63 (6). Since the area is the same as 10b and the flow was assumed incompressible, the pressure at 10c should only be the difference in pressure due to the loss across the butterfly valve. Therefore,

$$p_{10c} = p_{10b} - \Delta p_{10b-10c}$$

Between 10c and 10d exist a 90-degree elbow with a radius of one foot. The loss coefficient is found to be 20. Considering the material of this portion of the vacuum line

is cast iron, the friction factor is determined to be 0.05. The average Mach number

through this portion of the pipe is the same as at 10c since area is constant. By

calculating the change in pressure change due to losses from the 90 deg elbow,

the pressure at 10d is determined to be:

$$p_{10d} = p_{10c} - \Delta p_{10c-10d}$$

Lastly, the loss occurring 10d to PT11 is due to a sudden expansion. The area ratio is

0.163, which yields a loss coefficient of 0.75. The pressure at PT11:

$$p_{11} = p_{10d} - \Delta p_{10d-11}$$

which can be ready compared to the experimental data at PT11. The calculated pressure

and experimental data at PT11 can be compared graphically for a single run.

Appendix I: Analytical Investigation of Optical Cavity for Test #5
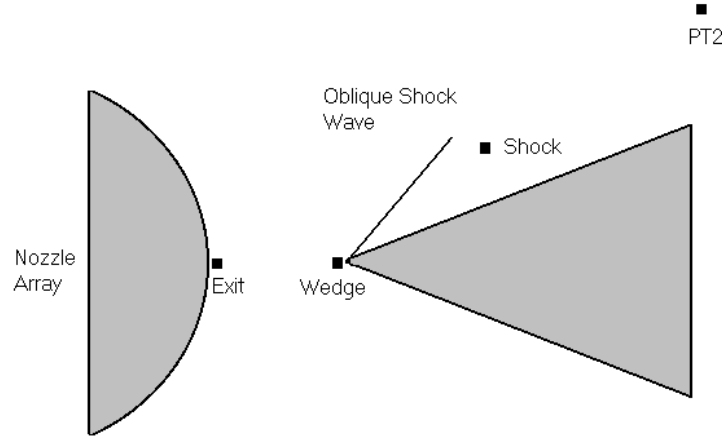
By using the labeled points above as calculation nodes, the pressures throughout the front diffuser area (through the optical cavity to PT2) were calculated. The beginning assumption was that an oblique shock wave existed and formed off the leading edge of the centerbody. The objective was to start with the reservoir pressure and calculate the pressure at the PT2 node. Then, compare the calculated pressure with the experimental data at this location. The nozzles were designed to accelerate the flow to $M_{exit} = 2.2$, which yields an isentropic static-to-stagnation pressure ratio of $\dfrac{p}{p_t} = 0.0935$. Initially, the flow through the nozzle array was assumed to be isentropic; therefore, the pressure at the exit plane of the nozzle was obtained:

$$p_{exit} = 0.0935 p_{t,reservoir}$$

However, the flow was not isentropic as was discussed in Appendix A. The Mach number at the exit plane of the nozzles was assumed to be 15% less than designed. Therefore, to better approximate the pressure at the nozzle exit:

$$p_{exit} = \frac{0.0935\, p_{t,reservoir}}{\left(1 + \frac{\gamma - 1}{2}(0.85 M_{exit})^2\right)^{\frac{\gamma}{\gamma - 1}}}$$

From the schlieren photographs, the Mach number at the centerbody can range from 1.9-2.7 (depending upon the procedure used). Assuming no losses between the 1.2-in distance from the nozzle exit plane to the leading edge of the centerbody, the pressure at the centerbody could be approximated by:

$$\frac{p_{wedge}}{p_{t,exit}} = f(M_{wedge})$$

Once again using the schlieren photos, the shock wave angle could be measured. The normal component of the velocity vector passing through the oblique shock wave was found by:

$$M_{wedge,n} = M_{wedge}\sin\theta$$

where the subscript n, indicates the normal component and θ was the shock wave angle. The pressure rise across a normal shock wave traveling at $M_{wedge,n}$:

$$\frac{p_{shock}}{p_{wedge}} = \frac{2\gamma M_{wedge,n} - (\gamma - 1)}{\gamma + 1}$$

This expression allows provided a solution for p_{shock}. The distance between the nodes "shock" and PT2 was small. Therefore, losses due to friction should be negligible, and the assumption was that $p_{PT2} = p_{wedge}$.

Normal Shock Wave
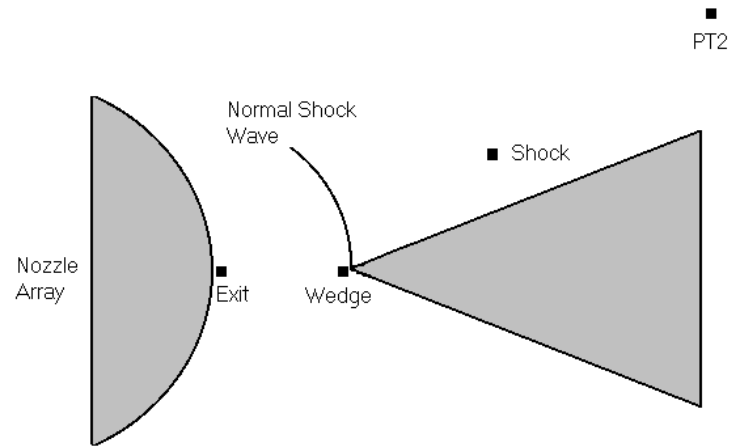
If the shock wave was assumed to be normal, then the calculation was performed the same as if oblique. The difference was the pressure rise across the shock wave. The normal component of the velocity at the wedge was not required.

Therefore,

$$\frac{p_{shock}}{p_{wedge}} = \frac{2\gamma M_{wedge} - (\gamma - 1)}{\gamma + 1}$$

M_{wedge} was obviously larger than its normal component. Consequently, p_{shock} would be greater. Both calculations of p_{PT2} based on shock shape could be graphically compared to the raw pressure data collected by experimentation.

Bibliography

1. Abramovich, G.N. <u>The Theory of Turbulent Jets</u>. Cambridge: M.I.T. Press, 1963.

2. Ames Research Staff. Equations, Tables, and Charts for Compressible Flow. Report No. 1135. Ames Aeronautical Laboratory, Moffett Field, CA.

3. Anderson, John D. <u>Gasdynamic Lasers: An Introduction</u>. New York: Academic Press, 1976.

4. Anderson, John D. <u>Modern Compressible Flow</u>. New York: McGraw-Hill, 1990.

5. Bjurstrom, David R. An Experimental Study of Clustered, Two-Dimensional Rocket <u>Nozzles</u>. Unpublished Thesis. Wright-Patterson, Ohio: Air Force Institute of Technology, 1984.

6. Fox, Robert W. and McDonald, Alan T. <u>Introduction to Fluid Mechanics, 4th ed</u>. New York: John Wiley and Sons, Inc., 1992.

7. Horkovich, J.A. Numerical Solutions for a Cylindrical Laser Diffuser Flowfield. Unpublished Dissertation. Wright-Patterson Air Force Base, Ohio: Air Force Institute of Technology, 1990.

8. John, James E.A. <u>Gas Dynamics, 2nd ed</u>. Upper Saddle River: Prentice Hall, 1984.

9. Mathieu, Jean and Julian Scott. <u>An Introduction to Turbulent Flow</u>. Cambridge: The Cambridge University Press, 2000.

10. Pai, Shih-I. <u>Fluid Dynamics of Jets</u>. Toronto: D. Van Nostrand Company, Inc, 1954.

11. Perram, Glen P. "Chemical Lasers", Web Page Tutorial. http://en.afit.edu/enp/Faculty/perram.html.

12. Schlichting, Hermann. <u>Boundary-Layer Theory, 6th ed</u>. New York: McGraw-Hill, 1968.

13. Shapiro, Ascher H. The Dynamics and Thermodynamics of Compressible Fluid <u>Flow, Vol 1</u>. New York: Ronald Press, 1953.

14. Taylor, Mark of TRW, Inc, Fluid and Thermophysics Department, Redondo Beach, CA. "Personal interviews," 2001.

15. Wheeler, Anthony J., Ganji, Ahmad R. Introduction to Engineering Experimentation. New Jersey: Prentice Hall, 1996.

16. Young, A.D. Boundary Layers. Washington DC: American Institute of Aeronautics and Astronautics, Inc, 1989.

17. Zucrow, Maurice J., Hoffman, Joe D. Gas Dynamics, Vol 1. New York: John Wiley & Sons, 1976.

18. Zumpano, F.D., Guile, R.N., Haas, M., Sobel, D.R. Radial Flow Diffuser Technology Program. UTRC R-84-958412-1, UTRC, East Hartford, CT., June 1984.

Vita

Captain Scott E. Bergren graduated from Western High School in Las Vegas, Nevada. He entered undergraduate studies at Florida State University in Tallahassee, Florida where he earned a Bachelor of Science degree in Mechanical Engineering in April 1997. He was commissioned through Detachment 145 AFROTC at Florida State University as a Distinguished Graduate.

His first assignment was at Travis AFB as an aircraft maintenance officer in May 1997. He was assigned to the 60th Equipment Maintenance Squadron where he served as Flight Commander. In August 2000, he entered the Graduate School of Engineering and Management, Air Force Institute of Technology. Upon graduation he will be assigned to the National Air Intelligence Center, Wright-Patterson AFB.

REPORT DOCUMENTATION PAGE

The public reporting burden for this collection of information is estimated to average 1 hour per response, including the time for reviewing instructions, searching existing data sources, gathering and maintaining the data needed, and completing and reviewing the collection of information. Send comments regarding this burden estimate or any other aspect of the collection of information, including suggestions for reducing this burden to Department of Defense, Washington Headquarters Services, Directorate for Information Operations and Reports (0704-0188), 1215 Jefferson Davis Highway, Suite 1204, Arlington, VA 22202-4302. Respondents should be aware that notwithstanding any other provision of law, no person shall be subject to an penalty for failing to comply with a collection of information if it does not display a currently valid OMB control number.
PLEASE DO NOT RETURN YOUR FORM TO THE ABOVE ADDRESS.

1. REPORT DATE (DD-MM-YYYY)	2. REPORT TYPE	3. DATES COVERED (From – To)
26-03-2002	**Master's Thesis**	Aug 2000-Mar 2002

4. TITLE AND SUBTITLE	5a. CONTRACT NUMBER
FABRICATION AND COLD-FLOW TESING OF SUBSCALE SPACE-BASED LASER GEOMETRY	5b. GRANT NUMBER
	5c. PROGRAM ELEMENT NUMBER
6. AUTHOR(S) Capt Scott E. Bergren	5d. PROJECT NUMBER
	5e. TASK NUMBER
	5f. WORK UNIT NUMBER

7. PERFORMING ORGANIZATION NAMES(S) AND ADDRESS(S)	8. PERFORMING ORGANIZATION REPORT NUMBER
Air Force Institute of Technology Graduate School of Engineering and Management (AFIT/ENY) 2950 P Street, Building 640 WPAFB OH 45433-7765	AFIT/GAE/ENY/02-3

9. SPONSORING/MONITORING AGENCY NAME(S) AND ADDRESS(ES)	10. SPONSOR/MONITOR'S ACRONYM(S)
SMC/TL, Attn: Capt Matthew Zuber 2420 Vela Way, Suite 1467-80 Los Angeles AFB, El Segundo, CA 90245-4659	11. SPONSOR/MONITOR'S REPORT NUMBER(S)

12. DISTRIBUTION/AVAILABILITY STATEMENT
APPROVED FOR PUBLIC RELEASE; DISTRIBUTION UNLIMITED.

13. SUPPLEMENTARY NOTES

.

14. ABSTRACT
The objectives of this research were to build a facility that could simulate the expected fluid flow properties in the conceptual Space Based Laser Integrated Flight Experiment (SBL IFX) gas dynamic laser using cold-flow, and to characterize the performance of the model. A $1/5^{th}$ scale model was fabricated and mated to a blow-down/vacuum wind tunnel. Using rapid data acquisition and schlieren photography the diffuser was determined to initially produce similar fluid flow to the SBL IFX, but rapidly became subsonic due to a transient normal shock wave formed when the wind tunnel was started.

15. SUBJECT TERMS
Space Based Laser, Supersonic Diffuser, Fluid Dynamics, Compressible Flow, Schlieren Photography, Blow-Down Wind Tunnel

16. SECURITY CLASSIFICATION OF:			17. LIMITATION OF ABSTRACT	18. NUMBER OF PAGES	19a. NAME OF RESPONSIBLE PERSON
a. REPORT U	b. ABSTRACT U	c. THIS PAGE U	UU	106	Dr Milton E. Franke (ENY)
					19b. TELEPHONE NUMBER (Include area code) (937) 255-3636 ext 4720